High-resolution retrieval of cloud microphysical properties and surface solar radiation using Himawari-8/AHI next-generation geostationary satellite

Husi Letu, Kun Yang, Takashi Y. Nakajima, Hiroshi Ishimoto, Takashi M. Nagao, Jerome Riedi, Anthony J. Baran, Run Ma, Tianxing Wang, Huazhe Shang, et al.

High-resolution retrieval of cloud microphysical properties and surface solar radiation using Himawari-8/AHI next-generation geostationary satellite

Husi Letu[a,b,*], Kun Yang[c], Takashi Y. Nakajima[b], Hiroshi Ishimoto[d], Takashi M. Nagao[e], Jérôme Riedi[f], Anthony J. Baran[g,k], Run Ma[h], Tianxing Wang[a], Huazhe Shang[a], Pradeep Khatri[i], Liangfu Chen[a], Chunxiang Shi[j], Jiancheng Shi[a]

[a] State Key Laboratory of Remote Sensing Science, The Aerospace Information Research Institute, Chinese Academy of Sciences (CAS), Datun Road No. 20 (North), Beijing 100101, China
[b] Research and Information Center (TRIC), Tokai University, 4-1-1 Kitakaname Hiratsuka, Kanagawa 259-1292, Japan
[c] Department of Earth Science System, Tsinghua University, Beijing 10084, China
[d] Meteorological Research Institute, Japan Meteorological Agency (JMA), Nagamine 1-1, Tsukuba 305-0052, Japan
[e] Earth Observation Research Center (EORC), Japan Aerospace Exploration Agency (JAXA), 2-1-1 Sengen Tsukuba-shi, Ibaraki 305-8505, Japan
[f] Laboratoire d'Optique Atmosphérique, Université de Lille–Sciences et Technologies, 59655 Villeneuve d'Ascq, France
[g] Met Office, Fitzroy Road, Exeter EX1 3PB, UK
[h] University of Chinese Academy of Sciences, Beijing 100049, China
[i] Center for Atmospheric and Oceanic Studies, Tohoku University, Sendai 980-8578, Japan
[j] National Meteorological Information Center, China Meteorological Administration, Beijing, China
[k] School of Physics, Astronomy and Mathematics, University of Hertfordshire, Hatfield, Hertfordshire AL10 9AB, UK

ARTICLE INFO

ABSTRACT

Optical properties of clouds and heavy aerosol retrieved from satellite measurements are the most important elements for calculating surface solar radiation (SSR). The Himawari-8/Advanced Himawari Imager (AHI) satellite measurements receive high spatial, temporal and spectral signals, which provides an opportunity to estimate cloud, aerosol and SSR accurately.

In this study, we developed the AHI official cloud property product (version 1.0) for JAXA P-Tree system. A look-up table (LUT) method was used to calculate high-temporal (10 min) and high-spatial (5 km) SSR from AHI cloud properties. First, the LUT of the SSR estimation was optimized through a radiative transfer model to account for solar zenith angle, cloud optical thickness (COT), effective particle radius (CER), aerosol optical thickness and surface albedo. Following this, COT and CER were retrieved from the AHI data, with ice cloud parameters being retrieved from an extended Voronoi ice crystal scattering database and water cloud parameters being retrieved from the Mie–Lorenz scattering model. The retrieved COT and CER for water clouds were compared well with MODIS collection 6 cloud property products, with correlation coefficients of 0.77 and 0.82, respectively. The COT of ice cloud also shows good consistency, with a correlation coefficient of 0.85. Finally, the SSR was calculated based on the SSR LUT and the retrieved cloud optical parameters. The estimated SSR was validated at 122 radiation stations from several observing networks covering the disk region of Himawari-8. The root-mean-square error (RMSE) at CMA (China Meteorological Administration) stations was 101.86 Wm^{-2} for hourly SSR and 31.42 Wm^{-2} for daily SSR; RMSE at non-CMA stations was 119.07 Wm^{-2} for instantaneous SSR, 81.10 Wm^{-2} for hourly SSR and 26.58 Wm^{-2} for daily SSR. Compared with the SSR estimated from conventional geostationary satellites, the accuracy of the SSR obtained in this study was significantly improved.

1. Introduction

Surface solar radiation (SSR) is an essential component of the Earth's energy budget. It is the downward solar flux at the surface, where the solar energy reaches the surface through the absorption and scattering of the atmosphere. SSR is also major driver for hydrological models and land surface models (Wild, 2009, 2012; Xue et al., 2013; He et al., 2015; Zhang et al., 2015; Huang et al., 2016a, 2016b; Tang et al.,

2016), which is important for solar resource assessment and photovoltaic power design. Ground-based stations measure accurate SSR with high temporal resolutions, but they are distributed sparsely. Because of this, it is difficult to produce spatiotemporally-continuous SSR from station data (Wang et al., 2012; Bao et al., 2018).

SSR values depend not only on the solar zenith angle (SZA), but also on optical properties of the cloud, aerosol and water vapor. Trace gases (e.g., O_3, O_2, CO_2) in the atmosphere also reduce SSR through Rayleigh scattering. However, the atmospheric loading of clouds and aerosols are the main parameters for affecting the spatial and temporal variation of the SSR. Satellite remote sensing is an efficient means to estimate these parameters, and has become the primary method to provide regional SSR (Takenaka et al., 2011; Lu et al., 2011; Qin et al., 2015; Bao et al., 2018). So far, geostationary and polar-orbiting satellite data have been widely used to estimate SSR. Geostationary satellites have high observation frequency compared with polar-orbiting satellites, and they are widely used to generate SSR products. The work of Pinker et al. (2002, 2003) developed a surface radiation budget product using the GOES-8 geostationary satellite data. In addition, the studies by Takenaka et al. (2011) proposed an artificial neural network (ANN)-based method to calculate the SSR with cloud microphysical properties retrieved from Multi-functional Transport Satellites (MTSAT) and Himawari-8 (H-8) geostationary satellite data (Damiani et al., 2018). On the other hand, some studies (Wang and Liang, 2009; Wang and Pinker, 2009; Huang et al., 2011; Qin et al., 2015) estimated high spatial-resolution SSR using the Moderate Resolution Imaging Spectroradiometer (MODIS) satellite measurements. The MODIS has advantages in monitoring cloud parameters and so yields highly-accurate SSR data with high spatial resolutions (Wang et al., 2015), but it cannot capture the diurnal variation of the SSR because of its low temporal resolution. Tang et al. (2016) attempted to improve the SSR accuracy through combining MODIS and MTSAT to retrieve cloud parameters. However, due to the limited channels of conventional geostationary satellites, the retrieval accuracy of cloud parameters still needs to be improved.

The Advanced Himawari Imager (AHI) instrument, carried on board the H-8 satellite, has 16 spectral bands with 0.5 km, 1 km and 2 km spatial resolutions from visible to thermal infrared regions. The temporal resolution is 10 min for the full disk observation region in East Asia. The observation capability of the AHI instrument is comparable to that of the GOES-R (Schmit et al., 2005) – another new-generation geostationary satellite. The H-8/AHI provides the possibility to observe the SSR with high accuracy and high spatiotemporal resolution (Bessho et al., 2016; Letu et al., 2018). However, a high-performance and fast-retrieval algorithm is required to retrieve cloud microphysical and optical parameters, while maintaining high accuracy, from a large amount of data from this advanced satellite.

There is a long history of development for SSR estimation from satellite data. Early studies (Klink and Dollhopf, 1986; Tarpley, 1979) used empirical algorithms that were established based on relationships between coincident satellite observed radiance and observed surface solar radiance. These algorithms cannot be extended from one region to another. In contrast, the Radiation Transfer Model (RTM) can calculate SSR more accurately, although the atmosphere in the model is assumed to be of a plane-parallel structure (Dedieu et al., 1987; Dubayah, 1992; Pinker and Ewing, 1985; Takenaka et al., 2011). However, this method is too computationally expensive to meet the requirement of rapid acquisition of SSR. Alternatively, some parameterization schemes based on the atmospheric radiative transfer were proposed to estimate SSR (Bisht et al., 2005; Duarte et al., 2006; Sridhar and Elliott, 2002; Yang et al., 2001a,b, 2006; Zhou and Cess, 2001; Zhou et al., 2007). These methods can greatly speed up the calculation, but at the expense of a certain amount of precision. Furthermore, another approach called Heliosat (Cano et al., 1986) and its more recent versions (e.g. Rigollier et al., 2000; Rigollier et al., 2004) are widely used to derive the SSR. One advantage of this approach is that the cloud effect can be directly retrieved from the satellite observations. A drawback of the method is
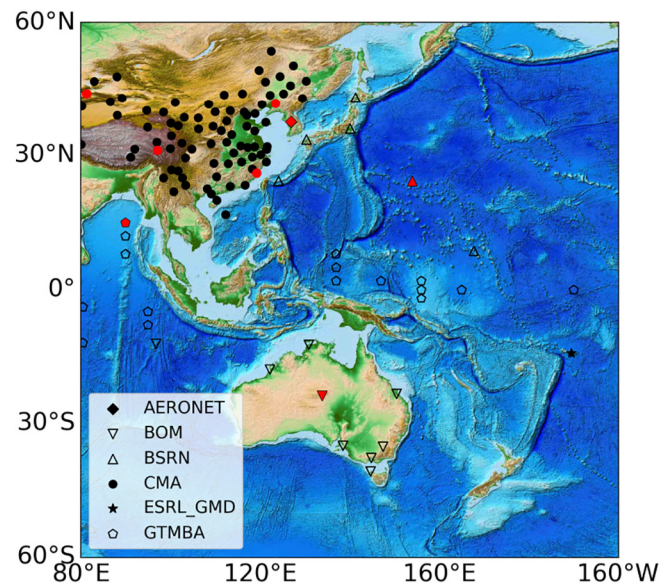

Fig. 1. Geographical distribution of ground observation sites for SSR validation.

that no microphysical cloud information is gained. To improve the computing efficiency without loss of accuracy, a variety of pre-calculated look-up table (LUT) algorithms were developed (Li et al., 1993; Liang et al., 2006; Tang et al., 2006; Tang and Li, 2008; Zheng et al., 2008; Wang and Liang, 2009; Wang and Pinker, 2009; Wang and Liang, 2009; Kim and Liang, 2010; Yan et al., 2016).

In addition to the SSR estimation algorithms, the accuracy of cloud microphysical properties (e.g. particle habit and size) is crucial when it comes to making highly-accurate estimations of SSR. Particularly, understanding ice crystal scattering (ICS) properties is essential for retrieving ice cloud optical parameters. However, ice cloud particles have various habits and sizes and their retrievals have significant uncertainties (Letu et al., 2016; Mei et al., 2018). In recent decades, numerous ICS models have been developed to retrieve ice cloud properties (Yang et al., 2000, 2005, 2013; Baran and Labonnote, 2007; Baran et al., 2014; C.-Labonnote et al., 2000, 2001; Doutriaux-Boucher et al., 2000; Ishimoto et al., 2010). Among them, the Voronoi ICS model was developed to produce the ice cloud product for the Second Generation Global Imager (SGLI)/Global Change Observation Mission-Climate (GCOM-C) (Ishimoto et al., 2012; Letu et al., 2012, 2016; Masuda et al., 2012; Nakajima et al., 2019), the AHI/H-8 (Letu et al., 2018; Shang et al., 2019) and Multi-Spectral Imager (MSI)/Earth Cloud Aerosol and Radiation Explorer (EarthCARE) satellite programs (Illingworth et al., 2015). The EarthCARE is to be launched in 2021. It was demonstrated that the Voronoi model can effectively retrieve the ice cloud properties from satellite measurements (Letu et al., 2016).

In this study, a new LUT-derived algorithm was developed to calculate all-sky SSR, based on the H-8/AHI data, which have high spatiotemporal and spectral resolutions. Specifically, the Voronoi ICS database was extended for the purpose of accurately deriving the ice cloud optical parameters, and their estimates were evaluated through comparing them with MODIS products. The forward RTM, together with the ICS database, was used to build the LUT utilized in the SSR estimation, and the SSR estimates from AHI were validated against widely-distributed station data.

2. Ground-based observation data

In this study, a total of 122 pieces of surface radiation observational data from 6 networks were used to validate satellite-derived SSR: 1 site from the Aerosol Robotic Network (AERONET) (Holben et al., 1998), 9 sites from the Australian Governments Bureau of Meteorology (BOM), 6
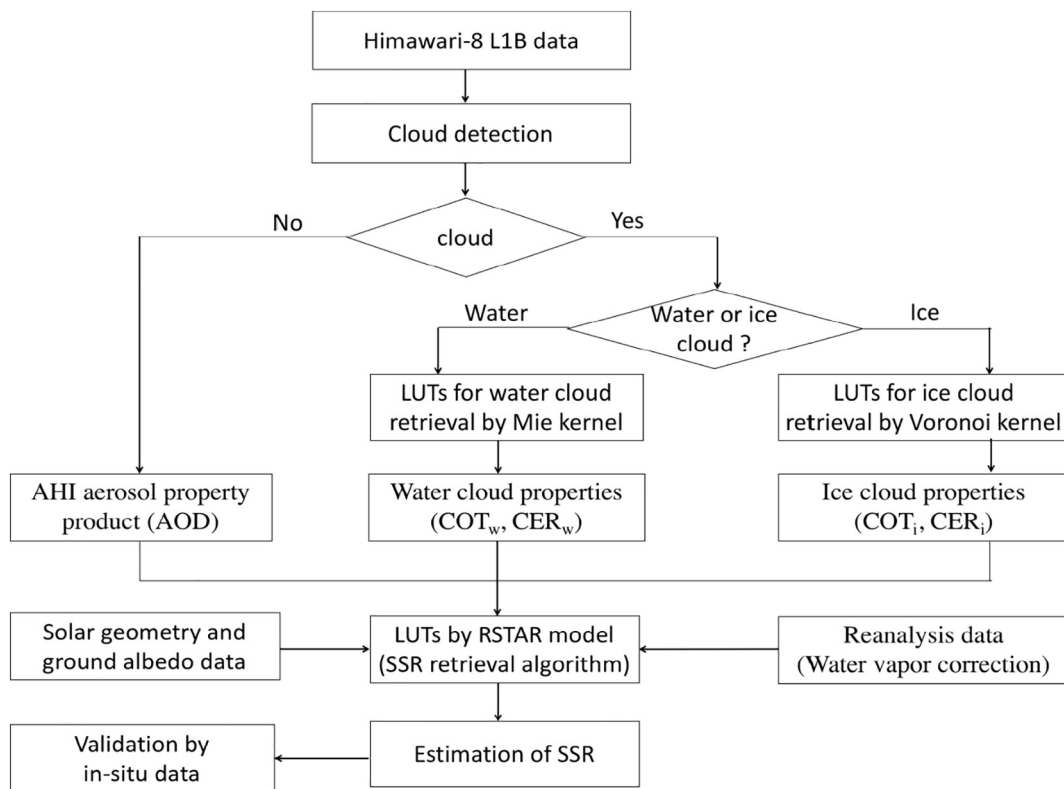
Fig. 2. Flowchart for calculating SSR from the AHI data.
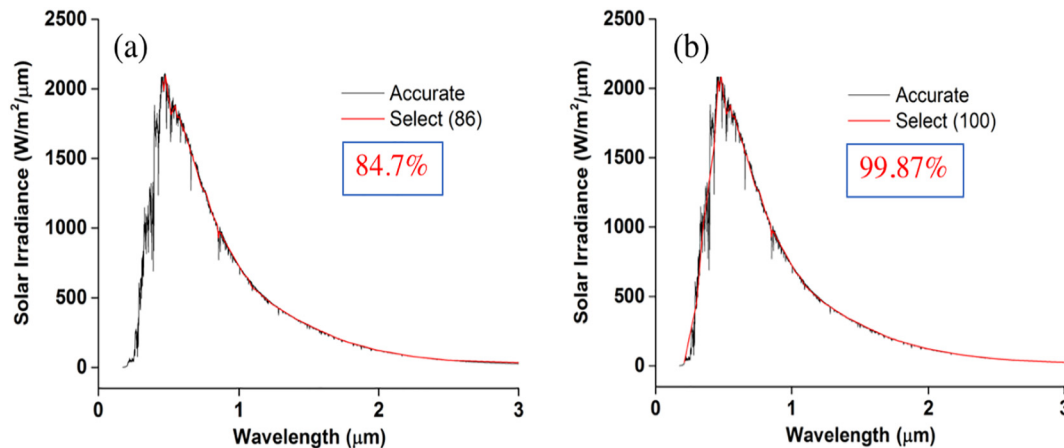
Fig. 3. Solar spectral irradiances as a function of the wavelength (black line), calculated using the ice refractive index data compiled by Warren and Brandt (2008): (a) the conventional Voronoi ICS model (red line) and (b) at the wavelengths of the new Voronoi ICS model (red line in Fig. 3b). (For interpretation of the references to color in this figure legend, the reader is referred to the web version of this article.)

Table 1
Input parameters and grid points of the variables used to build the LUT version of the CAPCOM.

Variables	Value range	No. of grid points	Unit
Solar zenith angle	0, 5, 10, 20, 30, 35, 40, 45, 50, 55, 60, 65, 70, 75, 80	15	degree
Satellite zenith angle	0, 5, 10, 20, 30, 35, 40, 45, 50, 55, 60, 65, 70, 75, 80	15	–
Azimuth angle	0, 10, 20, 30, 40, 50, 60, 70, 80, 90, 100, 110, 120, 130, 140, 150, 160, 170, 180	19	–
Water cloud optical thickness	0.2, 0.5, 1, 2, 3, 4, 5, 8, 12, 17, 23, 31, 41, 54, 70, 80, 90, 100	18	–
Water cloud effective particle radii	4, 7, 9, 11, 14, 17, 22, 30, 38, 46, 54, 62	12	μm
Ice cloud optical thickness	0.1, 0.5, 1, 2, 4, 8, 16, 32, 48, 64, 80, 90, 100, 110, 120, 130, 140, 150	18	–
Ice cloud effective particle radii	5, 10, 20, 40, 60, 80, 100, 110, 120, 130, 140, 150	12	μm

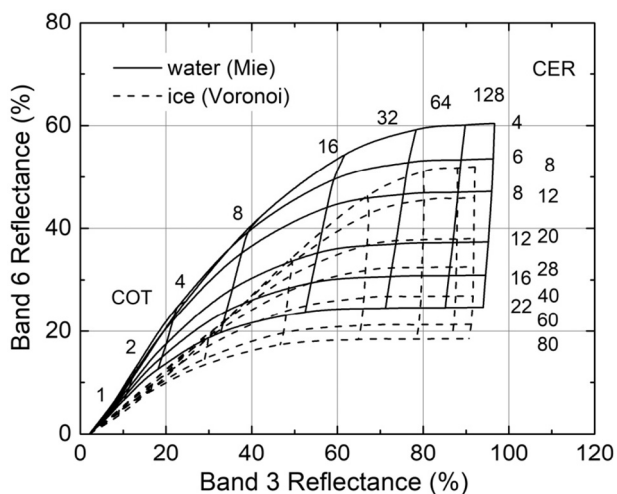**Fig. 4.** Simulated reflectance of the water and ice clouds at weakly-absorbing channel (center wavelength at 0.64 μm) and absorbing channel (center wavelength at 2.25 μm) of the AHI measurements (SZA = 30°, SatZA = 30°, RAA = 60°).

sites from the Baseline Surface Radiation Network (BSRN) (Driemel et al., 2018), 1 site from the Earth System Research Laboratory Global Monitoring Division (ESRL_GMD) (Bruhwiler and Dlugokencky, 1970), 16 sites from the Global Moored Buoy Array (GTMBA) (Mangum, 1998), and 89 sites from China Meteorological Administration (CMA) radiation stations. The above 122 sites are located in a variety of climate zones, and Fig. 1 shows the spatial location of the aforementioned sites. All of the stations, except the CMA stations, provide high temporal resolutions (1–3 min) of radiation data, and SSR estimates were validated at the individual sites.

3. Development of the retrieval algorithm

In this study, we improved the cloud property retrieval algorithm and updated the product from the beta version to the formal version
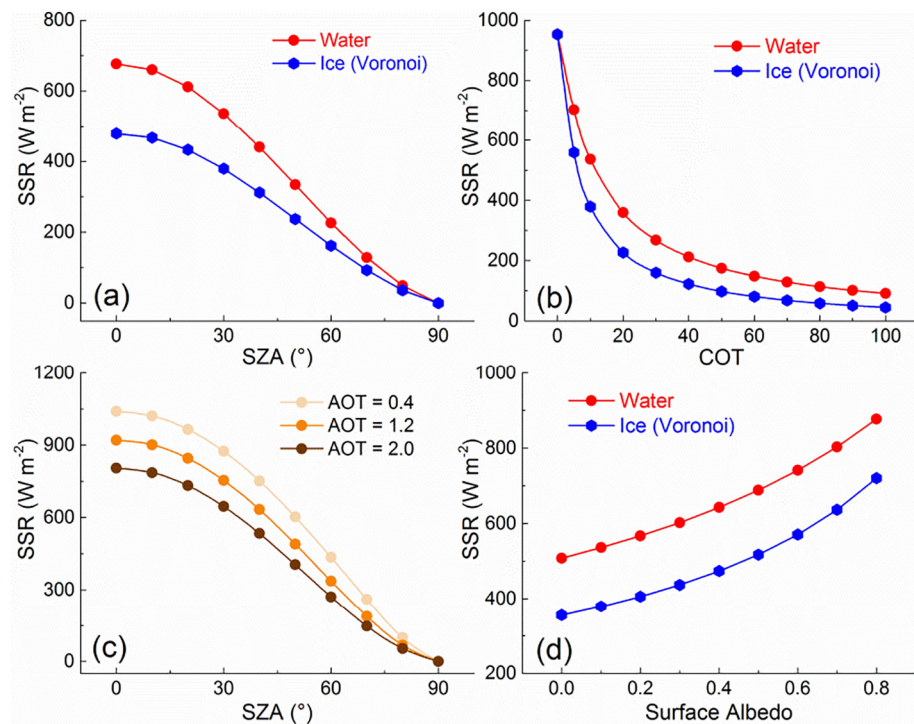
1.0, which included some improvements of the ice cloud microphysical properties. The official cloud property product (beta version) was released on JAXA P-Tree system in September 2016 (https://www.eorc.jaxa.jp/ptree/). This work was introduced in our recently-published paper (Letu et al., 2018). Fig. 2 shows the SSR estimation algorithm in the present study. There are two LUT algorithms used for retrieving cloud parameters and SSR, respectively. The retrieval procedure is as follows:

(1) Identify the sky conditions (clear or cloudy), by utilizing a cloud screening algorithm (Ishida and Nakajima, 2009), from the AHI L1B data.
(2) For clear sky, the aerosol optical thickness (AOT) official AHI level 2 (L2) product (Yoshida et al., 2018; Kikuchi et al., 2018) is used in the SSR algorithm.
(3) For the cloudy sky, we first determine the cloud phase using the brightness temperature (BT) band and differences between two BT bands (Baum et al., 2000). To retrieve cloud optical thickness (COT) and cloud effective radius (CER), the Mie-Lorenz scattering model is used if the cloud is identified as a water cloud, and the Voronoi ICS is used if the cloud is ice. The cloud parameters are retrieved based on a LUT algorithm, whose input is the AHI-observed reflectance at center wavelength of λ = 0.64 μm and 2.3 μm. The details of the ICS model and the retrieval algorithm are provided in Section 3.2.
(4) With the input of the estimated cloud and aerosol optical parameters, the SSR is estimated through the SSR algorithm, which is based on a forward RTM called RSTAR (Nakajima and Tanaka, 1986, 1988; Sekiguchi and Nakajima, 2008). The details of the RSTAR are introduced in Section 3.1.

3.1. The RSTAR model

The RSTAR model is used to establish the LUTs for the purpose of retrieving the SSR from AHI measurements. The RSTAR model is a package of numerical models specializing in atmospheric radiative transfer that is applicable to the plane-parallel atmosphere, and the calculated wavelengths can cover 0.17–1000 μm. The presumed plane-parallel atmosphere can be divided into 50 layers, from the sea surface

Fig. 5. a Variations of the SSR with SZA for water and ice clouds, with conditions for water cloud (COT = 10, CER = 8 μm, As = 0.1) and ice cloud (COT = 10, CER = 32 μm, As = 0.1). b Variations of the SSR with COT for water and ice clouds, with conditions for water cloud (CER = 8um, SZA = 30°, As = 0.1) and ice cloud (CER = 32um, SZA = 30°, As = 0.1). c Variations of the SSR with SZA and aerosol optical thickness (AOT), with conditions for aerosol model assumed to be of the rural type and As = 0.1. d Variations of the SSR with As for COT and CER of the water cloud (COT = 10, CER = 8 μm, SZA = 30°) and ice cloud (COT = 10, CER = 32 μm, SZA = 30°) (Atmospheric model: U.S. standard atmosphere).

Table 2
Grid points of the variables used to build the LUT algorithm of SSR.

Variables	Value range	Increment	No. of grid point	Unit
Solar zenith angle	0–70, 80, 90	2.0	38	Degree
Aerosol optical thickness	0–3	0.25	13	–
Water cloud optical thickness	0–60, 80, 100, 150	2.5	28	–
Water cloud effective particle radii	4, 8, 16, 32, 64	–	5	μm
Ice cloud optical thickness	0–40, 80, 100, 150	2.5	20	–
Ice cloud effective particle radii	4, 8, 16, 32, 64, 128, 150	–	7	μm
Surface albedo	0–0.8	0.2	6	–
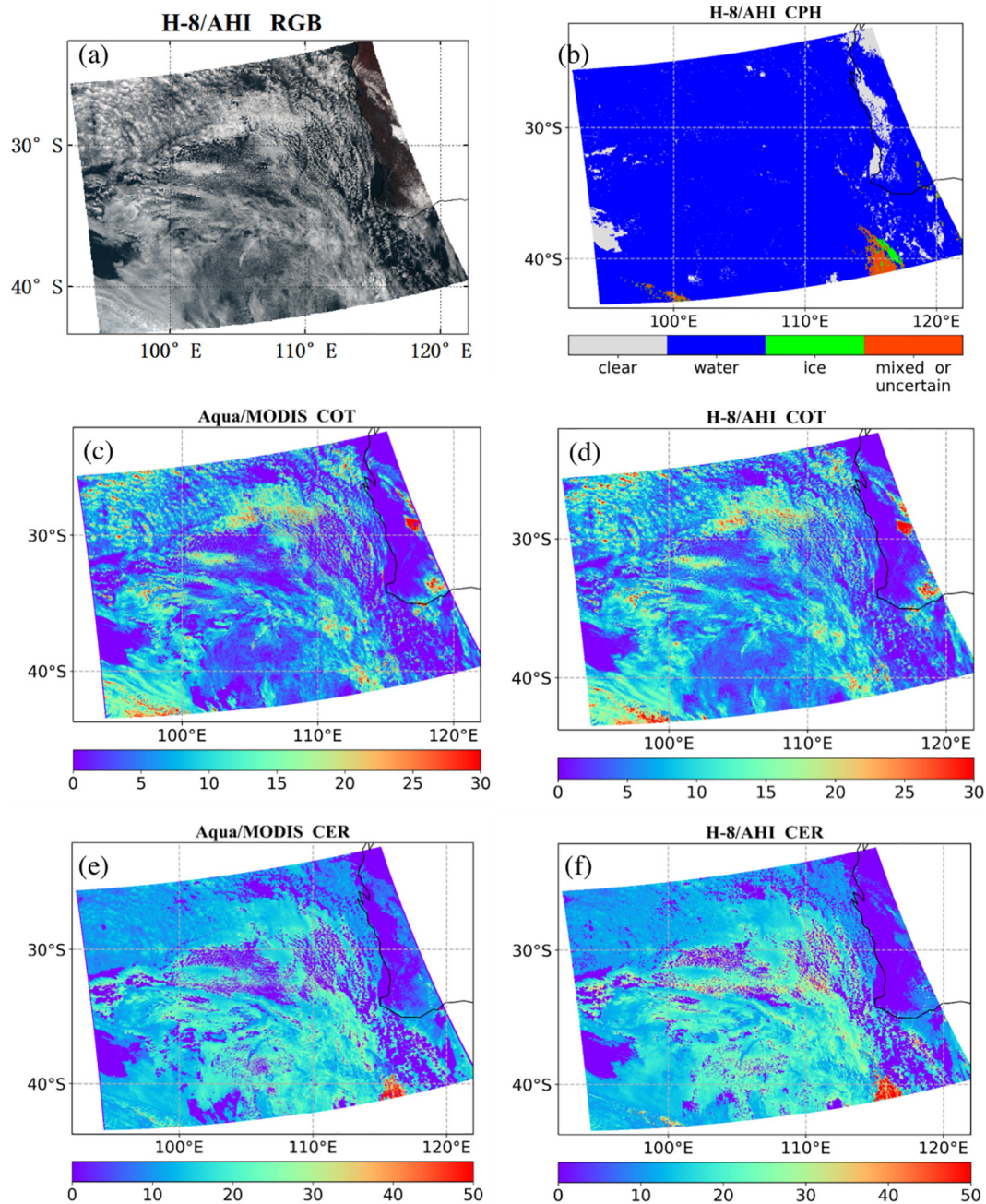
Fig. 6. Comparison of retrieved optical parameters for water cloud. a AHI true color composition image. b Cloud phase. c COT from MODIS C6 at 02:45 UTC, November 12, 2018. d COT from the AHI. e CER from MODIS C6. f CER from the AHI at 02:50 UTC, November 12, 2018.
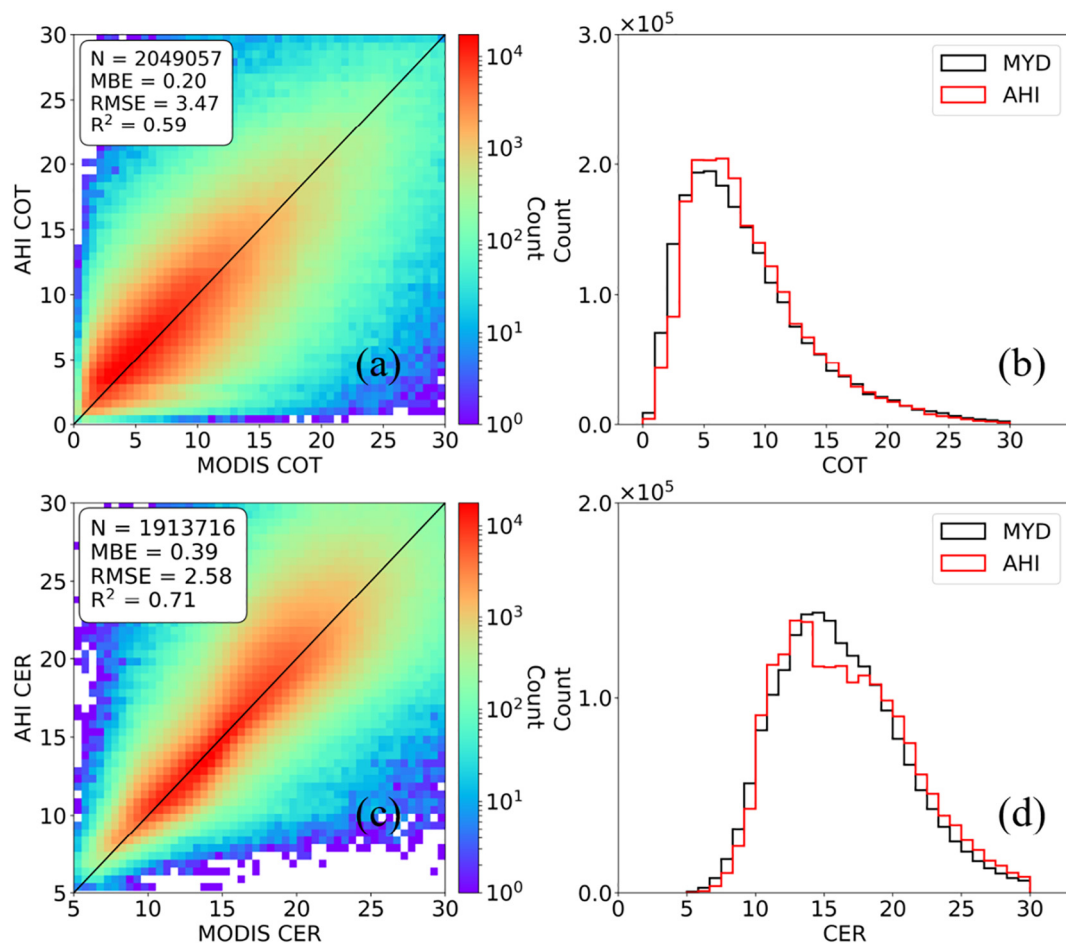
Fig. 7. Scattering plot (a and c) and the histograms (b and d) of CER and COT from MODIS C6 (MYD) and AHI data in the selected area as presented in Fig. 6.

level to the highest altitude of 120 km, and 6 atmosphere models can be selected. The plane-parallel atmosphere includes 11 classes of aerosol models that are composed of seven basic components (Sekiguchi and Nakajima, 2008).

The cloud particle scattering model in the RSTAR is composed of water and ice clouds. The ice cloud model further consists of various ice scattering kernels, such as spherical and ellipsoidal shapes and hexagonal columns. In this study, we installed the Voronoi ICS model into RSTAR as a new ice scattering kernel to retrieve the ice cloud properties from the AHI data.

3.2. Extension of Voronoi ICS database

The conventional Voronoi ICS model consists of single-scattering properties (e.g. phase function, single-scattering albedo, asymmetry factor, absorption efficiency, extinction efficiency) at 86 spectral wavelengths that were selected to retrieve the optical properties of the ice clouds (Letu et al., 2018). The selected wavelengths in the Voronoi ICS model are determined by the variation of the refractive index of ice in the satellite observation bands. They can satisfy the requirement of accurate estimation of ice cloud parameters from satellite measurements, e.g. MODIS, AHI, SGLI and MSI (Letu et al., 2018), but need an extension in order to estimate SSR accurately. Fig. 3 shows the solar spectral irradiation (SSI) at the wavelengths of the Voronoi ICS model calculated using the refractive index data provided by Warren and Brandt (2008). The integral SSI at the wavelengths of the conventional Voronoi model accounts for 84.7% of the accurate SSR (Fig. 3a). This implies that the number of wavelengths utilized by this Voronoi model is not enough to calculate the surface SSR. In the present study, we

enlarged the number of spectral wavelengths to calculate the single-scattering properties of the Voronoi ISC model from 86 to 100 and installed them in the RSTAR model as an ice scattering kernel. From Fig. 3b, we can confirm that the solar irradiation over the selected 100 wavelengths (red line) of the new Voronoi ISC model is highly consistent with the accurate data (black line), i.e. the calculated solar irradiation produced by the new Voronoi model accounts for 99.87% of the accurate total solar irradiance. With the extended ICS database, the RSTAR is used to construct the LUT of the SSR estimation.

3.3. Cloud parameter retrieval

A LUT algorithm was developed using the "Comprehensive Analysis Program for Cloud Optical Measurement" (CAPCOM) to retrieve the cloud properties (e.g. COT and CER). CAPCOM is a comprehensive cloud property retrieval package (Nakajima and Nakajma, 1995; Kawamoto et al., 2001). One component included in the package is a forward model called CAPCOM-fwd, which is essentially the same as RSTAR. The RSTAR module is a comprehensive radiative transfer package designed for multiple purposes. The CAPCOM-fwd is more convenient for constructing the LUT of the cloud property retrievals.

As shown in Fig. 2, a cloud screening algorithm is used to identify cloudy and clear pixels from AHI L1B data (Letu et al., 2014, 2018; Shang et al., 2017; Ishida et al., 2018). Water and ice cloud phases are also detected in this process. CAPCOM-fwd is used to build the LUT for establishing the AHI cloud properties retrieval algorithm. Input parameters (Table 1) include observation geometries, COT and CER for the water and ice cloud phases. They are optimized to reduce the computational cost without loss of accuracy. The radiance at AHI band with
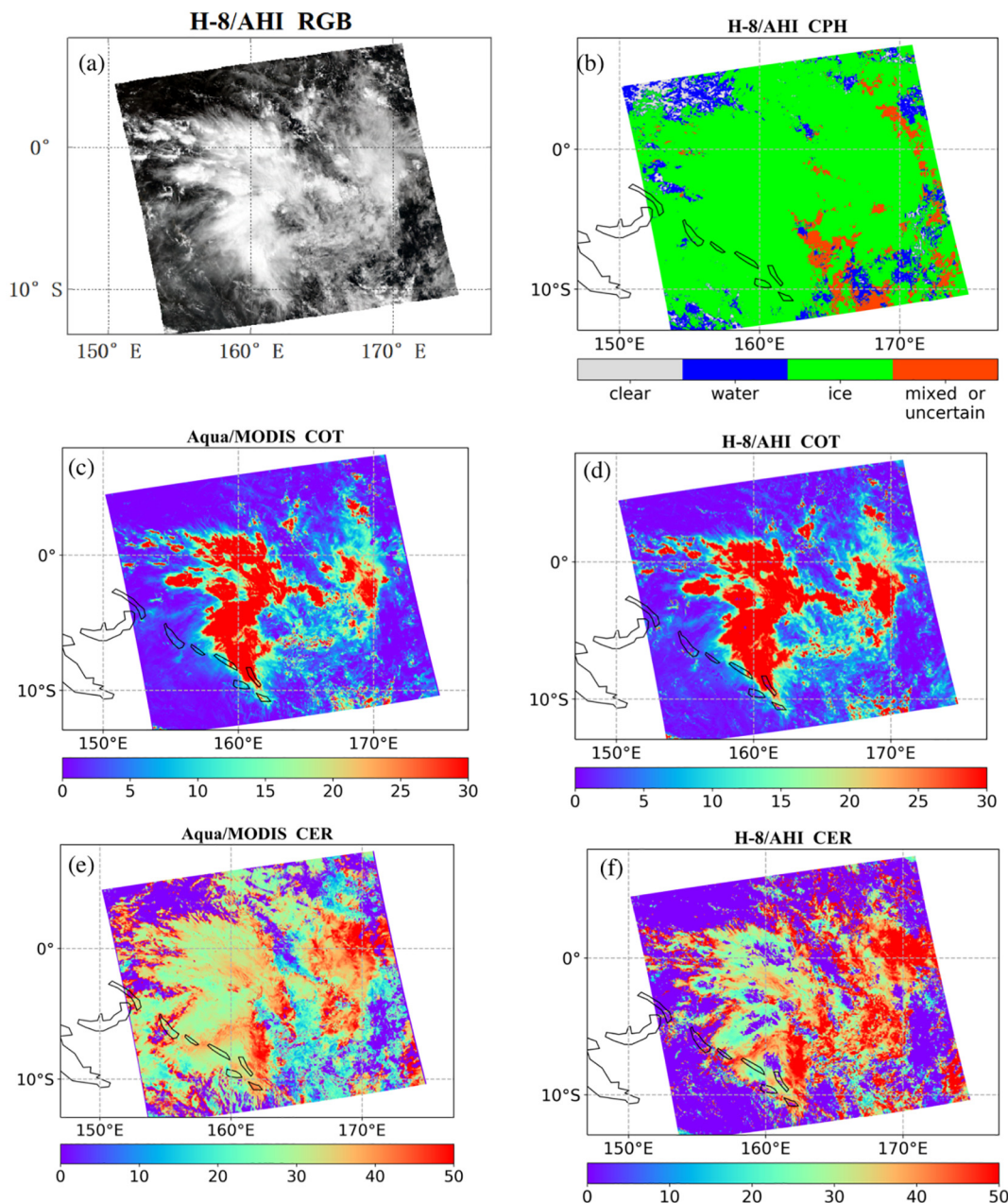
Fig. 8. Similar to Fig. 6, but for ice cloud. a AHI true color composition image. b Cloud phase. c COT from MODIS C6. d COT from the AHI. e CER from MODIS C6. f CER from the AHI at 02:50 UTC, November 11, 2018.

center wavelength of 0.64 μm and 2.3 μm are the input parameters. The Mie–Lorenz scattering database installed in the CAPCOM-fwd is used to establish the water cloud LUT. The Voronoi ICS database installed in the CAPCOM-fwd is employed to establish the ice cloud LUT. Based on the LUT, the Newton–Raphson method is used to find the solution of two cloud parameters (COT and CER) from AHI band 3 and band 6. Detailed descriptions of the cloud retrieval algorithm are introduced in Nakajima and Nakajma (1995) and Letu et al. (2018).

The CER and particle size distribution (PSD) is a main cloud microphysical parameter to be retrieved. The Log-normal distribution function is used to represent the PSD of both the water and ice clouds. The CER and PSD for the water cloud are defined by Eqs. (1) and (2), respectively (Nakajima and Nakajma, 1995).

$$r_e = \frac{\int_0^\infty r^3 n(r) dr}{\int_0^\infty r^2 n(r) dr},$$

(1)

where n(r) indicates the PSD. Log-normal distribution is used in the calculations.

$$n(r) = \frac{N}{\sqrt{2\pi}\sigma} exp\left[\frac{-(ln(r_e/r_0))^2}{2\sigma^2}\right],$$

(2)

where r_0 and σ are the mode radius and standard deviation of the cloud particle, respectively.

The definition of the CER for the beta version of AHI official ice cloud products is given by Eq. (3), which was introduced by Letu et al. (2018). In this study, we employed Eq. (4) to define the CER and thus improve the AHI ice cloud retrieval algorithm. The improved algorithm was applied in version 1.0 of the AHI cloud products, which was released by Japan Aerospace Exploration Agency (JAXA) in December 2018 (https://www.eorc.jaxa.jp/ptree/). Eq. (4) uses the projected area of the Voronoi single particle to define the ice cloud CER.
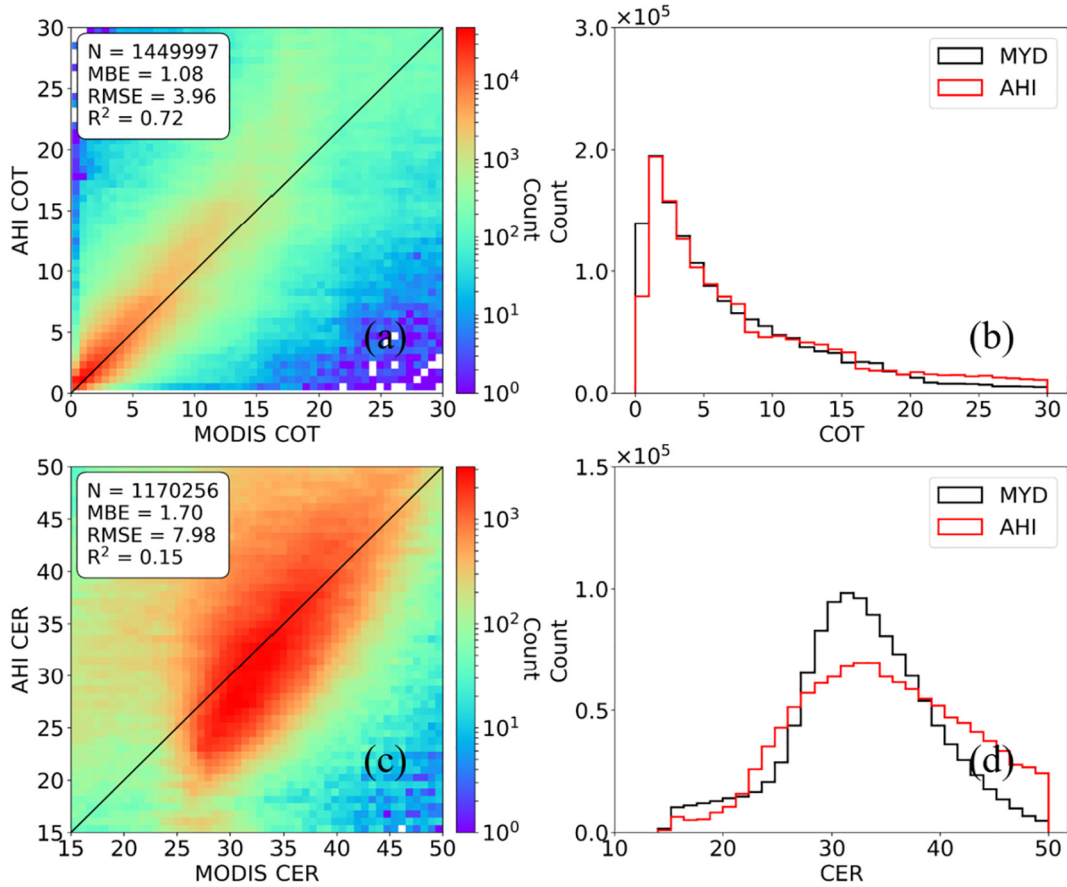
Fig. 9. Similar to Fig. 7, but for ice cloud at 06:50 UTC, September 11, 2018.

$$R_{eff} = \frac{3}{4} \frac{\int_0^\infty Vol(L) n(L) dL}{\int_0^\infty A_{eqa}(L) n(L) dL}, \quad (3)$$

$$R_e = \frac{3}{4} \frac{\int_0^\infty Vol(L) n(L) dL}{\int_0^\infty A_{prj}(L) n(L) dL}, \quad (4)$$

where $Vol(L)$ and $A_{eqa}(L)$ are the volume and area of an equivalent volume sphere of a Voronoi particle, respectively; $A_{prj}(L)$ is the projected area of the randomly-oriented Voronoi single particle; L and $n(L)$ are the maximum dimension and PSD of the ice crystals, respectively.

Fig. 4 shows simulation results of the satellite-observed reflectance at AHI band 3 (center wavelength at 0. 64 μm) and band 6 (center wavelength at 2.3 μm) as a function of various COT and CER, according to the Mie–Lorenz scattering model and Voronoi ICS model applied in the RSTAR. The results show that the reflectance for water and ice cloud models are significantly different as a function of COT and CER, because of different single-scattering and microphysical properties between water and ice cloud particles. Therefore, it is important to differentiate the water and ice cloud properties, respectively, to ensure accurate calculation of the SSR.

3.4. LUT for SSR calculation

The RSTAR model is used to calculate the SSR from AHI data-derived cloud and aerosol properties. The RSTAR is a narrow-band radiative transfer model, and therefore the SSR is calculated by integrating the radiative flux over the spectral wavelengths. In this study, the Voronoi new scattering database with 100 spectral wavelengths was installed in the RSTAR to calculate the radiative flux for ice clouds. These wavelengths were determined by the characteristics of the

refractive index and SSI in the spectral wavelength when developing the scattering database. The calculation of the radiative flux from AHI measurements by the RTM requires a large amount of computational time. Moreover, the AHI data contains a large number of pixels due to its high spatial-temporal resolution. Therefore, we developed a pre-calculated LUT-based algorithm to estimate the SSR from the AHI measurements.

The sensitivity analysis was performed using the RSTAR model to optimize the most important parameters for calculation of the SSR, which includes SZA, AOT, COT, CER and surface albedo (As). The sensitivity of each of the parameters in the calculation of the SSR is shown in Fig. 5. The SSR changes greatly from approximately 478 Wm^{-2} and 677 Wm^{-2} to 0 Wm^{-2} as a function of SZA ranging over 0°–90° for ice and water clouds, respectively (Fig. 5a). The SSR drastically changes from around 960 Wm^{-2} to 100 Wm^{-2} and 200 Wm^{-2} with COT ranging over 0–40, but relatively smoothly when COT varies from 40 to 100 for ice and water clouds, respectively (Fig. 5b). Fig. 5c shows the variation of SSR for different AOTs with the increase of SZA. When the SZA is equal to 0, the effect of the AOT changes on SSR is most obvious. When AOT increases from 0.4 to 2.0, the SSR decreases from 1050 Wm^{-2} to 760 Wm^{-2} for SZA = 0. In this study, AOD information about aerosols is used in the calculation of the SSR, which is of great significance to improve the calculation accuracy of SSR. However, not only the AOD, but also the aerosol type has a significant impact on the calculation. At present, there are still some shortcomings in the estimation of AOD, and types of passive observation satellite data, which will lead to uncertainty in the SSR calculation, this being also the limitation of the current aerosol algorithm in the calculation of the SSR. Fig. 5d shows the effect of As on SSR, which indicates that SSR changes from 508 Wm^{-2} and 356 Wm^{-2} to 877 Wm^{-2} and 720 Wm^{-2} with As ranging over 0 to 0.8 for water and ice clouds, respectively.
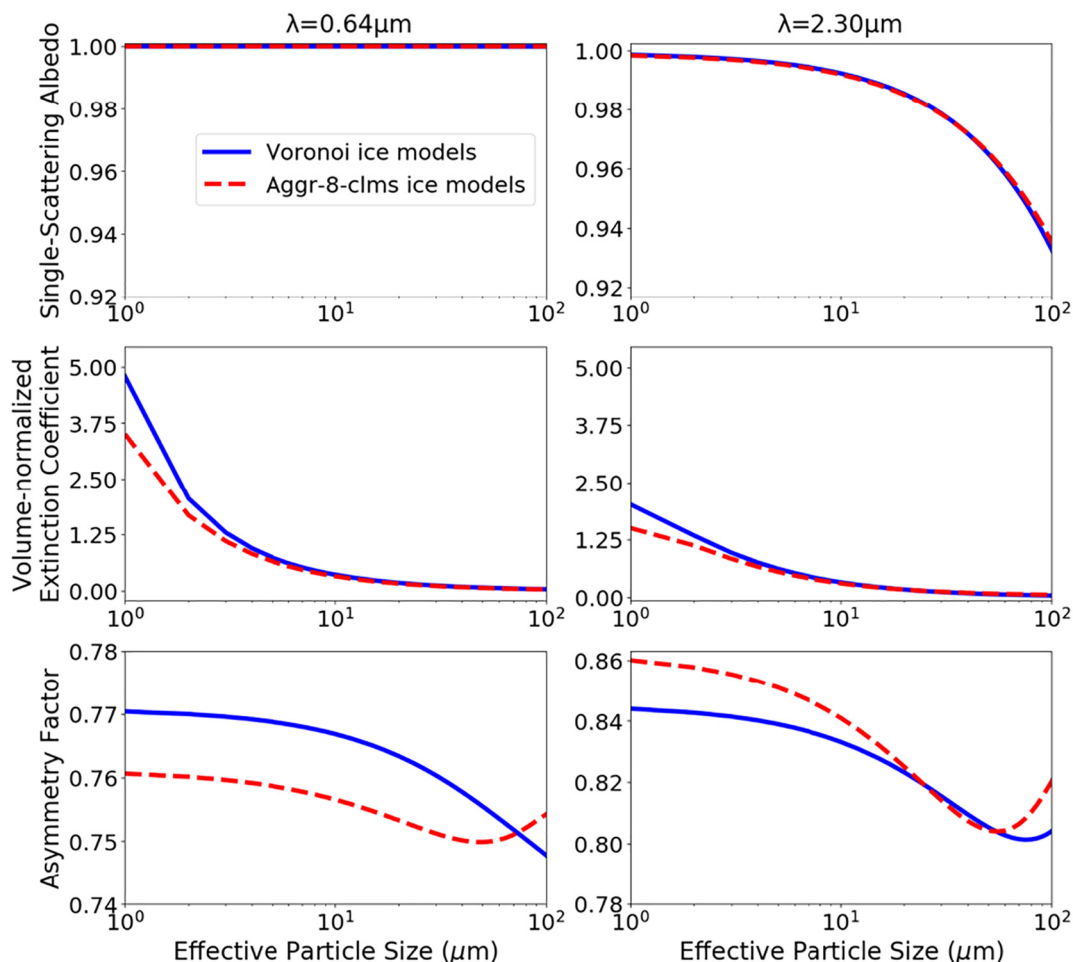
Fig. 10. Comparison of single scattering albedo, volume-normalized extinction coefficient and asymmetry factor for bulk-scattering properties of ice particle models at the wavelengths of 0.64 μm and 2.3 μm as a function of the parameter size.

High values of As can bring multiple scattering effects between surface and atmosphere, and thus the surface can receive more downward solar radiation. According to the above sensitivity analysis, we constructed an optimal LUT, whose grid points for each of the input variables are shown in Table 2. Furthermore, the water vapor effect on SSR is significant and varies spatiotemporally, but the LUT uses a standard atmosphere. Therefore, this effect is corrected through the water vapor effect parameterization in Yang et al. (2006) using ERA-Interim re-analysis water vapor data.

4. Validations

4.1. Cloud property retrievals

Cloud is highly variable in the vertical scale, and the CER can also vary substantially in a cloud. However, such vertical information is not assumed in the radiative transfer model and retrieval algorithms, and thus leads to uncertainties in the final retrievals. The MODIS-derived COT and CER are two of the satellite cloud products with a long time series, high precision and high reliability, even though they also have considerable uncertainties (Platnick et al., 2003, 2017). To investigate the accuracy of the AHI cloud retrievals, we compared them with cloud property retrievals from the MODIS collection 6 (MODIS C6) product (Platnick et al., 2017). Fig. 6 shows the AHI true color composition image, cloud phase, COT and CER (2.1 μm) from MODIS C6 and the AHI Ver 1.0 cloud property product at 02:50 UTC, on November 12, 2018. Fig. 6a shows the cloud distribution in the selected area. The area is almost completely occupied by water clouds (Fig. 6b). The spatial

distribution of the COT from MODIS C6 (Fig. 6c) and AHI data (Fig. 6d) are comparatively consistent. The distribution of CERs from the AHI data (Fig. 6f) is also consistent with MODIS C6 (Fig. 6e). Fig. 7 illustrates the comparisons of COT and CER by showing the scattering plot and histogram in the area as presented in Fig. 6. The COT from the AHI data is also consistent with results from MODIS C6, with a coefficient of determination (R^2) of 0.59, mean bias error (MBE) of 0.2 and root-mean-square error (RMSE) of 3.47. Similarly, CER from the AHI data is also well correlated with MODIS C6 results. The R^2, MBE and RMSE are 0.71, 0.39 μm and 2.58 μm in the selected areas, respectively.

Fig. 8 is similar to Fig. 6, but for the time of 02:45 UTC, November 12, 2018. In this case, most of the area in the image is covered by ice cloud (Fig. 8b) rather than water cloud. Spatial distributions of the COT and CER from the AHI data (Fig. 8d and f) are comparable to that from the MODIS C6 product (Fig. 8c and e). The bright region in Fig. 8a corresponds to high COT (red color area) in Fig. 8c and d. Fig. 9a and b also indicate good correlations of the COT between AHI and MODIS C6, with R^2 of 0.72, MBE of 1.08, and RMSE of 3.96. From Fig. 8e, f, Fig. 9c, and d, we can see that CER of the ice cloud from the AHI data is generally larger than the MODIS C6 retrievals, except for CERs ranging from 25 to 40 μm. The R^2, MBE and RMSE are 0.15, 1.7 μm and 7.98 μm in the selected areas, respectively. A possible reason for this is the radiance calibration error for the AHI measurement, as well as the differences in the single-scattering properties of the assumed ice particle models used in the AHI and MODIS cloud products. A study by Okuyama et al. (2018) pointed out that the radiance calibration error of the AHI data has little effect on COT and CER retrievals. It can be inferred that the different ice scattering models used in AHI and MODSI

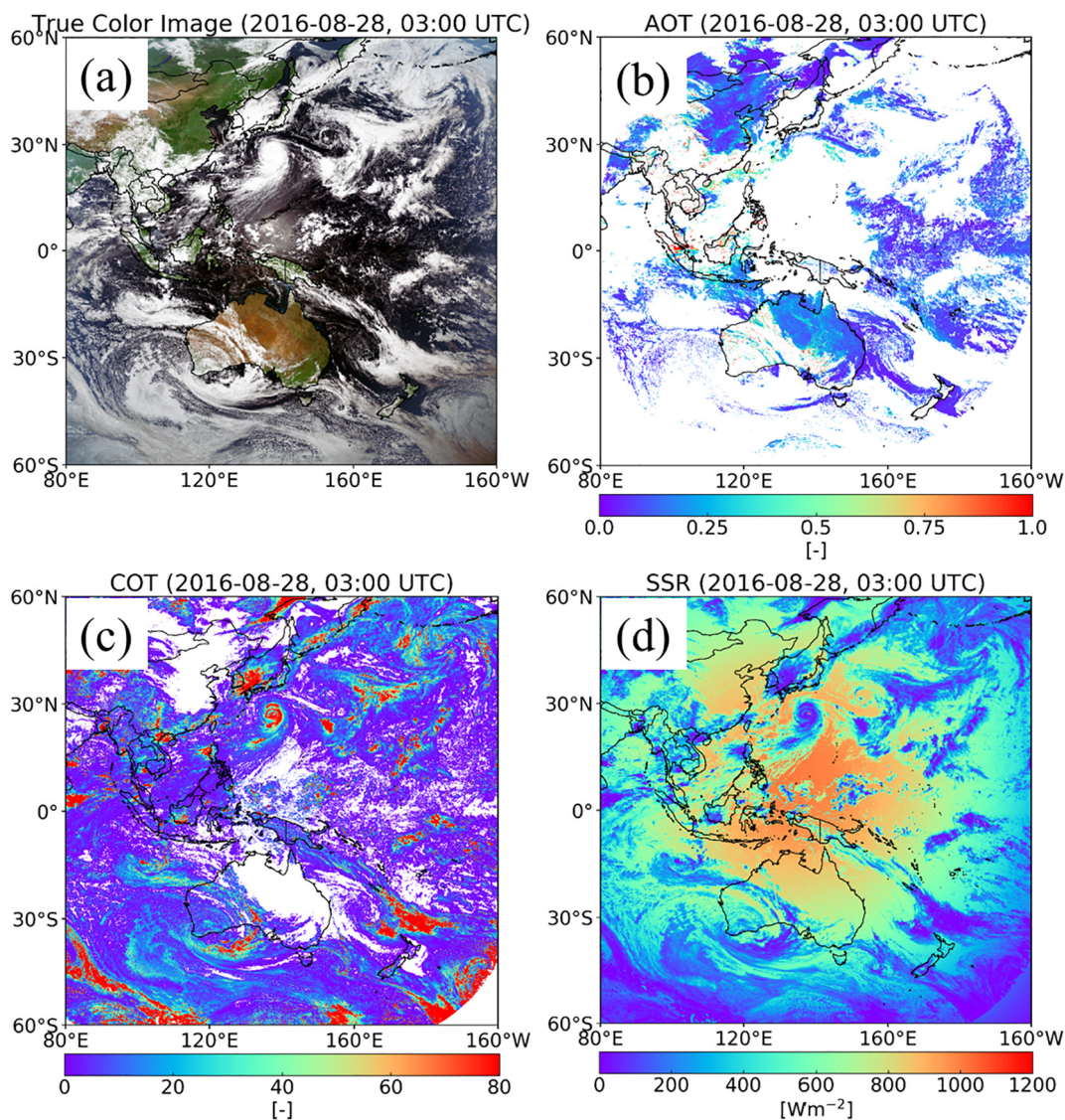**Fig. 11.** a True color composition. b AOT. c COT. d SSR estimation result in the full disk region of the AHI measurement for 03:00 UTC, August 28, 2016.
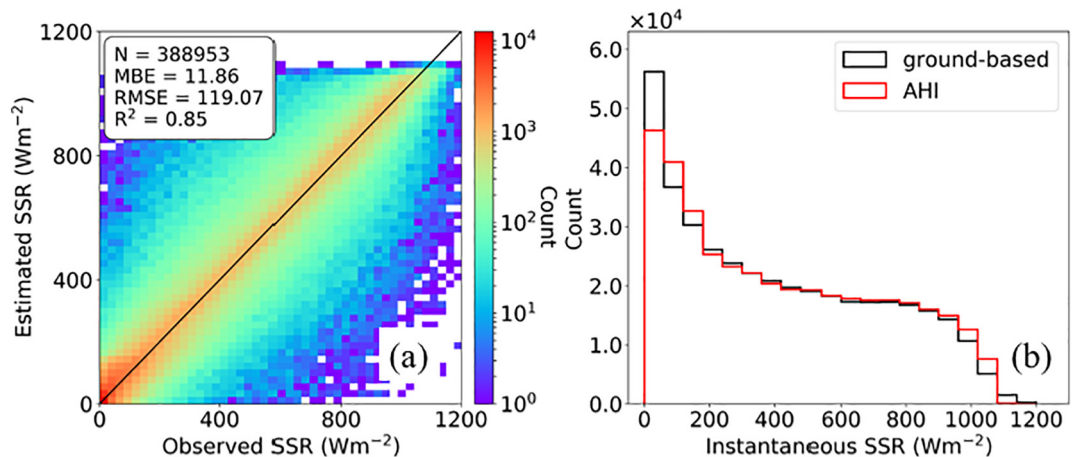

Fig. 12. a): Scattering plot of the estimated and observed instantaneous SSR, b): PDF of the instantaneous SSR between AHI estimated results and ground observations at 33 non-CMA stations in 2016, except for the months of January, February and June.
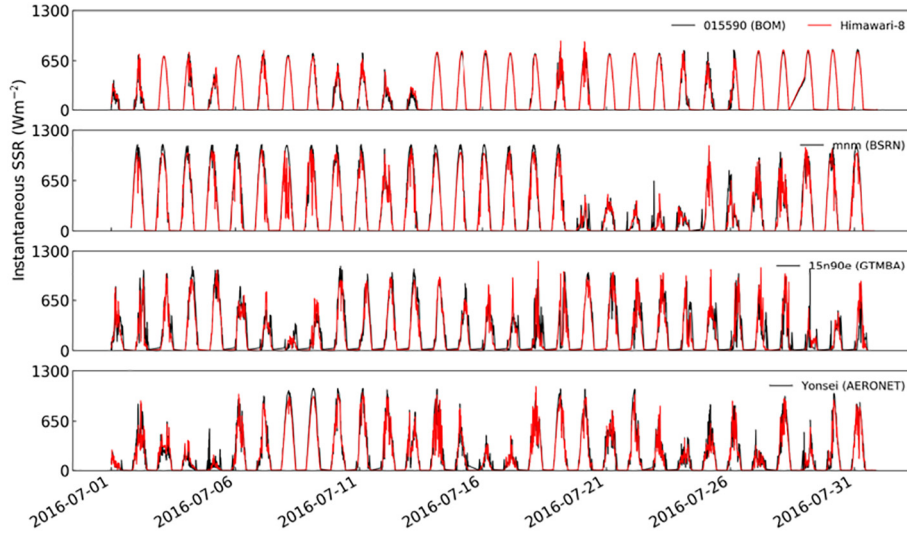
Fig. 13. Comparison of the instantaneous SSR from AHI estimated results and ground observations for July 2016 (UTC) at four sites in Fig. 1 (red symbols). (For interpretation of the references to color in this figure legend, the reader is referred to the web version of this article.)
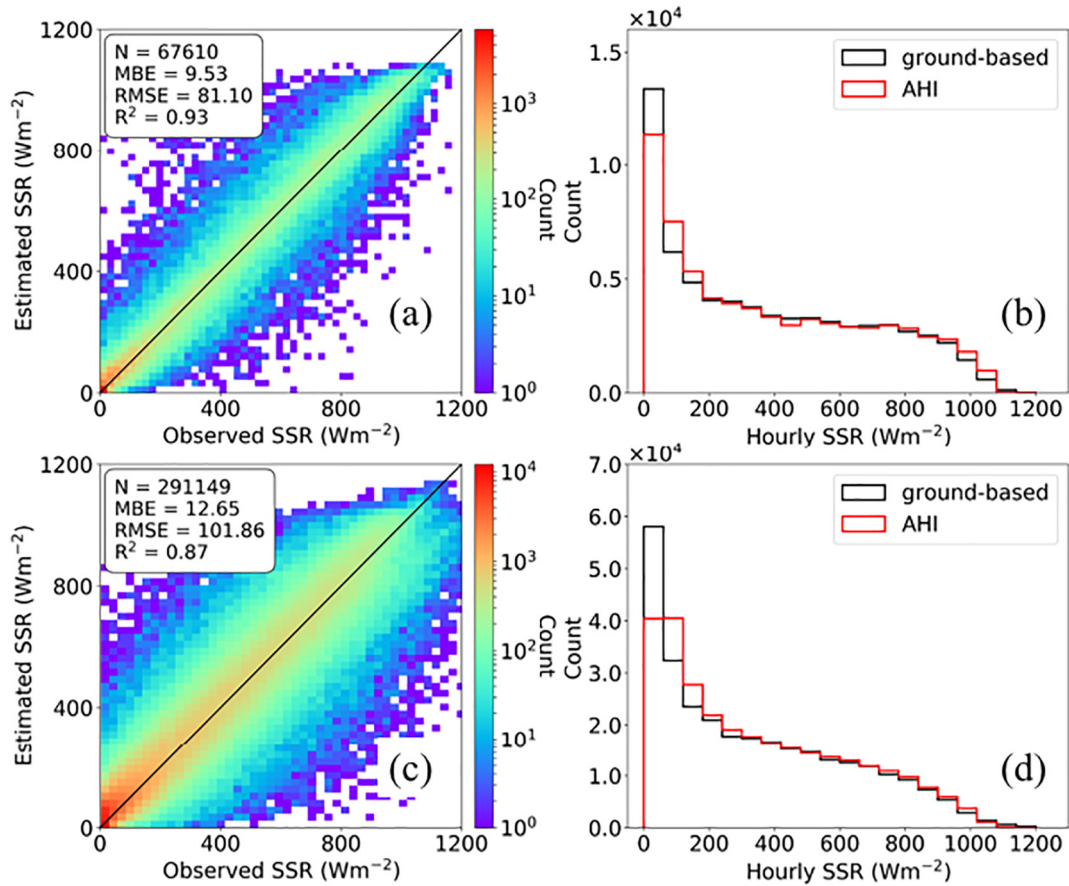
Fig. 14. Comparison of the hourly SSR between AHI estimated results and ground observations for the non-CMA (a and b) and the CMA stations (c and d).

cloud products have resulted in these differences. To investigate the influence of the different ice scattering models on the ice cloud retrievals, we compared the bulk scattering properties of the Voronoi and 8-solid column aggregates with severe roughness (8-agg-cl) (Platnick et al., 2017) at wavelength of 0.64 μm and 2.3 μm as a function of effective parameter size (EPS). EPS is defined as twice the value of CER found from Eq. (4). From Fig. 10, it can be seen that the single scattering albedo of the two models is similar and relatively consistent.

However, there are obvious differences between the volume-normalized extinction coefficient (Eqs. (5), (6); Yang et al., 2001a,b) for small particles (about EPS < 10 μm) and the asymmetry factors of the two models, which may lead to differences in COT retrievals between the two products.

$$\bar{\beta}_{ext}(\lambda) = \int_{D_{min}}^{D_{max}} Q_{ext}(D,\lambda)A(D)n(D)dD \tag{5}$$
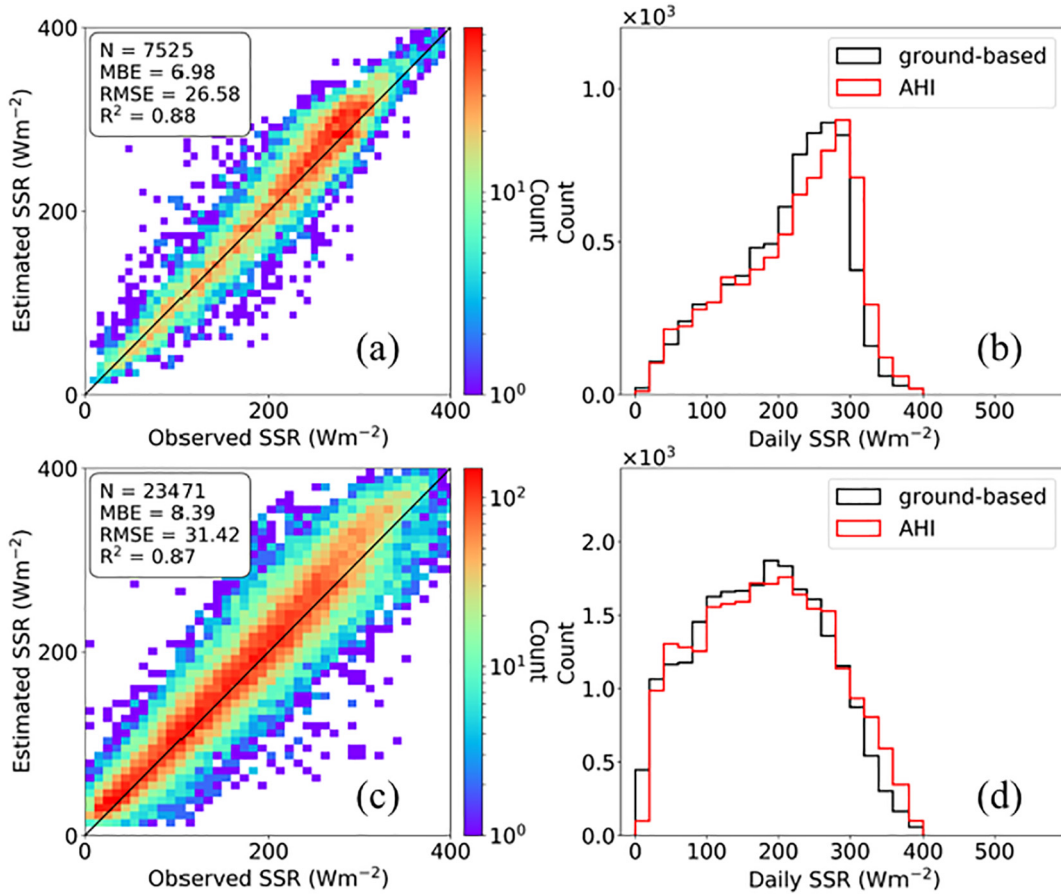
Fig. 15. Same as Fig. 14, but for daily SSR validation results of the non-CMA (a and b) and CMA stations (c and d).

$$\widetilde{\beta}_{ext}(\lambda) = \frac{\overline{\beta}_{ext}}{IWC} = \frac{\int_{D_{min}}^{D_{max}} Q_{ext}(D,\lambda)A(D)n(D)dD}{\rho_{ice} * \int_{D_{min}}^{D_{max}} V(D)n(D)dD} \qquad (6)$$

where D is particle maximum dimension, D_{min} and D_{max} are the minimum and maximum ice particle dimensions, V and A are the volume and area of an ice particle, n is the number distribution, Q_{ext} is the extinction efficiency of an ice particle. $\overline{\beta}_{ext}$ is the bulk extinction coefficients, ρ_{ice} is the solid density of ice, IWC is the ice water content, $\widetilde{\beta}_{ext}$ is the IWC-normalized extinction coefficients.

4.2. Validation of the SSR from AHI

A total of 122 radiation stations, shown in Fig. 1, were used to evaluate the estimated SSR. Among them, a total of 33 radiation stations provided high temporal resolution SSR of 1–3 min and were used to evaluate instantaneous, hourly, and daily SSR estimates. A total of 89 CMA radiation stations provided hourly mean SSR, and they were used to validate the hourly and daily SSR estimates. The three metrics of MBE, RMSE, and R^2 were used to test the performance of the estimated SSR. However, it is necessary to point out the characteristics of the satellite data and ground-based observation data. The ground observation data at the radiation stations represent the SSR value at a point. However, the SSR estimated by the satellite represents the average SSR of a pixel (5×5 km^2). This observation feature is also a limitation of the satellite product validation.

4.2.1. Validation of instantaneous SSR estimates

First, we show the spatial distribution of SSR in a severe weather condition. Fig. 11 presents SSR estimation results from H-8 data with near full disk regions for 03:00 UTC, August 8, 2016. In the true color

image (Fig. 11a), a typhoon near Japan can clearly be seen. Fig. 11b and c show the spatial distribution of AOT and COT in the full disk region. Fig. 11d illustrates the estimated SSR. It is indicated that SSR decreases drastically with increasing COT; high values of SSR with lower SZA can also be seen.

H-8/AHI has a high temporal resolution of 10 min, and thus here we adopted 10 minute-averaged SSR observations to evaluate the instantaneous SSR from the satellite data. Since CMA stations do not have instantaneous observation data, we evaluated AHI-derived SSR using the 33 non-CMA stations. Fig. 12a presents comparisons of instantaneous SSR between AHI estimated results and ground observations at 33 non-CMA stations in 2016 except for the months of January, February, and June. The instantaneous SSR from the AHI data are highly consistent with the ground-based observation data, with R^2 of 0.85. The MBE and RMSE values at these 33 sites are 11.86 Wm^{-2} and 119.07 Wm^{-2}, respectively. Fig. 12b shows the probability density function (PDF) of the SSR in Fig. 12a. From the figure, we can confirm that the PDF of the estimated SSR (red line) is consistent with the result of the ground-based SSR. Fig. 13 shows comparisons of instantaneous SSR at four randomly selected stations. Clearly, high temporal variability of SSR is retrieved well.

4.2.2. Validation of hourly SSR estimates

Fig. 14 shows the hourly mean SSR validation results at the non-CMA and CMA stations. Both the non-CMA and CMA SSR validation results show a high consistency between the satellite-derived SSR and the ground observation data. For the non-CMA stations (Fig. 14a and b), a total of 33 sites show R^2 and RMSE values of 0.93 and 81.1 Wm^{-2}, respectively. For CMA stations (Fig. 14c and d), a total of 89 sites show R^2 and RMSE values of 0.87 and 101.86 Wm^{-2}, respectively. The PDF of the two SSRs for the non-CMA and CMA stations also illustrates good
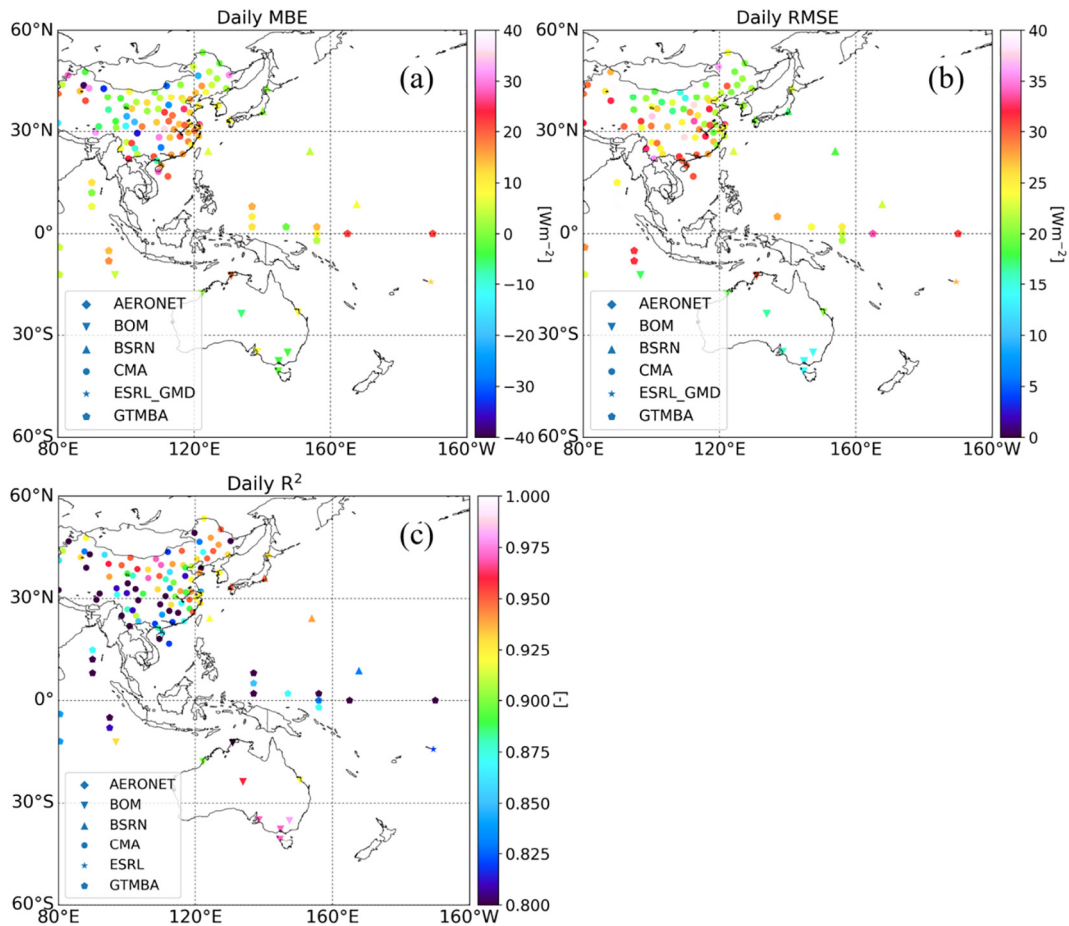
Fig. 16. a): MBE, b): RMSE, c): R^2 for daily SSR at all ground stations in 2016, except the months of January, February, and June. Symbols with different shapes mean a different network; the color bar shows the daily mean MBE, RMSE and R^2 values.
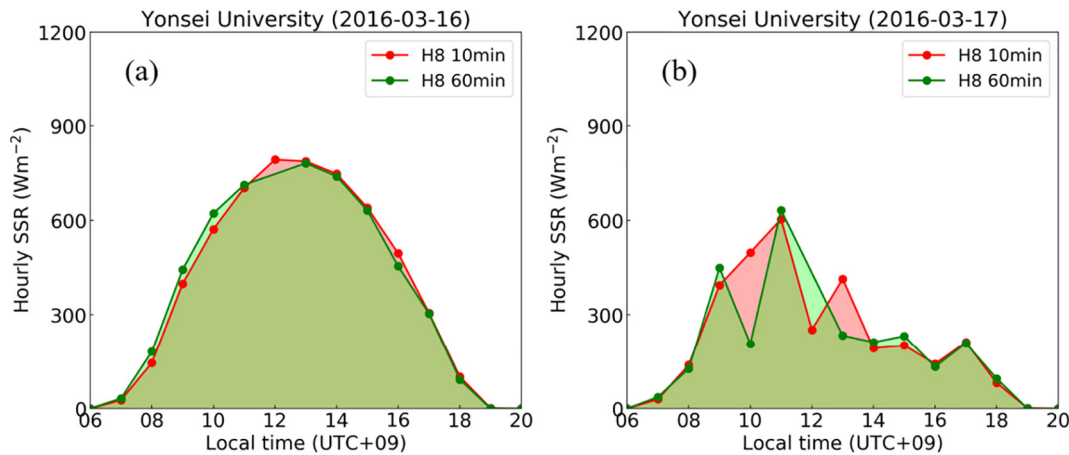
Fig. 17. Comparison of SSR from hourly mean and hourly interval data at Yonsei University site on a clear day (March 29, 2018) and a cloudy day (March 7, 2018).

consistency, as shown in Fig. 14b and d.

4.2.3. Validation of daily SSR estimates

Fig. 15 shows the scattering plot and PDF of the daily mean SSR between AHI estimated results and ground-based observation data at the non-CMA (Fig. 15a and b) and CMA stations (Fig. 15c and d). The non-CMA stations show R^2 and RMSE values of 0.88 and 26.58 Wm^{-2}, while the CMA values are 0.87 and 31.42 Wm^{-2}, respectively. The RMSE value at CMA stations is less than the one found by Tang et al. (2016) (34.2 Wm^{-2}), who combined MTSAT measurements and MODIS

atmospheric products to estimate SSR over China at all CMA stations. Moreover, the RMSE of our daily mean SSR is significantly smaller than the results produced by Jia et al. (2013), who used FY-2C data to estimate SSR with a RMSE of 49.3 Wm^{-2} over China. These results indicate that SSR estimation in the present study works well in various climate regions.

Fig. 16 shows the MBE, RMSE and R^2 values for daily mean SSR at all ground stations. Different symbols represent different networks. Most of the MBE values are positive and large positive values are mainly located in South China and the sea surface (Fig. 16a). Tang et al. (2016)

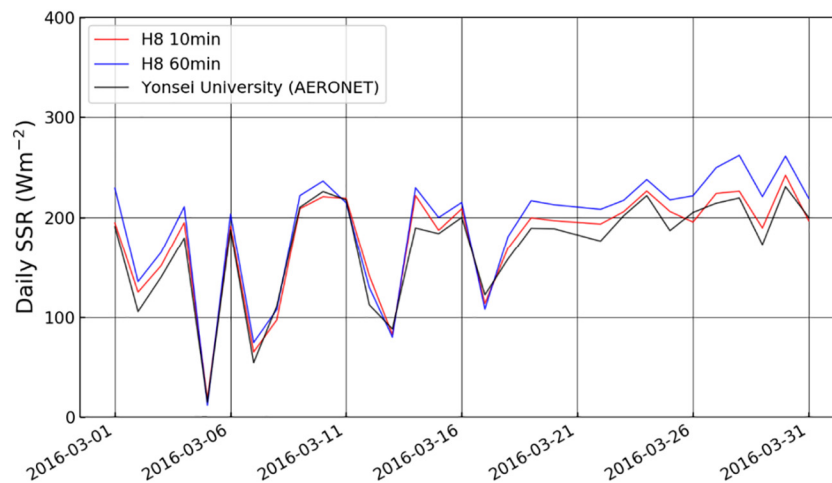**Fig. 18.** Comparison of daily SSR between high temporal (SSR_10min) and hourly interval (SSR_60min) against in-situ measurements (Yonsei University) for March 2016.

Table 3

Comparison of daily SSR values between high temporal (SSR_10min) and hourly interval (SSR_60min) against in-situ measurements at Yonsei University station for March 2016.

Yonsei University	MBE (Wm^{-2})	RMSE (Wm^{-2})	R^2
H8 10min	7.1	20.0	0.94
H8 60min	20.0	25.0	0.77

reported that the higher SSR biases in South China are due to dense and frequent cloud cover in this subtropical continental region, and this was also confirmed by Li et al. (2004) by time-series ISCCP data and cloud observation data. As shown in Fig. 16b, RMSE values are smaller in most parts of China's mid-high latitudes (north of 30°N) and Australia, < 25 W/m². The RMSE values in southern China, southwestern mountain areas and the equatorial waters of South Asia are higher than those in northern China mentioned above – probably larger than 25 W/m². The R^2 in Fig. 16c also shows similar spatial distributions to those of MBE and RMSE, but they are inverted. The accuracy of the estimated SSR depends not only on the calculation algorithm, but also on the accuracy of trace gases, water vapor, retrieved aerosol and cloud parameters, such as AOT, COT, and CER. When the accuracy of the above parameters is high enough, the RMSE error in Fig. 16b mainly comes from the matching of satellite data and ground-based observation, as well as the accuracy of ground-based data itself. From Fig. 16, we can also confirm that the spatial distribution of RMSE and R2 is obviously different each other. We consider that different surface types and complex terrain areas lead to the poor matching between the satellite calculated SSR, and the ground observation data. The SSR estimated by the satellite is the averaged value over the space of 5 × 5 km (1 pixel), but the ground observation is a point of data. The large difference between the observation point and the surrounding surface type or the distribution of stations in the complex terrain area will reduce the representativeness of the observation site to the satellite observation range, resulting in the above differences.

5. Discussions

SSR products with a high temporal resolution can be used to drive land surface models that usually need hourly or sub-hourly radiation data. AHI has a 10-minute observation frequency, which is essential for monitoring variations of the SSR. Here we discuss how the AHI high observation frequency may improve the accuracy of SSR estimation. Taking the Yonsei University site as an example, Fig. 17 shows hourly

variations of SSR for a clear day and a cloudy day. In the figure, SSR_10min is the average of six retrievals of SSR instantaneous value from AHI within 1 h, and the SSR_60min is a single SSR instantaneous value from AHI within 1 h. Their difference shows the role of observation frequency in the retrieval. The difference between SSR_10min and SSR_60min is small for the clear sky (Fig. 17a), but the difference is considerably large under the cloudy sky (Fig. 17b). Fig. 18 shows the comparison of daily SSR data at this station in March 2016 among the observations, the 10-min retrieval mean and the 60-min retrieval mean. It can be found that the degree of agreement between the ground observation data and SSR_10min is high, with MBE, RMSE and R^2 of 7.1 Wm^{-2}, 20.0 Wm^{-2} and 0.94, respectively (in Table 3). These error metrics indicate much better accuracy than the SSR_60min that yields MBE, RMSE and R^2 of 20.0 Wm^{-2}, 25.0 Wm^{-2}, and 0.77, respectively. Therefore, the AHI high temporal resolution is of great significance for improving the SSR retrieval accuracy.

6. Conclusions

In this paper, surface solar radiation (SSR) was estimated from H-8/AHI new-generation geostationary satellite measurements produced by the LUT-based algorithm. Cloud properties derived from AHI measurements were used to calculate the SSR from the proposed algorithm. However, the accuracy of calculated SSR depends largely on the reliability of cloud parameters. The calculation process of the SSR includes two major steps.

The first step was the retrieval of cloud properties. A cloud property retrieval algorithm was established to calculate the COT and CER for water and ice clouds as input data to the SSR calculation algorithm. The Voronoi ice crystal scattering database was improved to retrieve the AHI ice cloud properties. The retrieval results of the COT and CER from the AHI data were validated by comparing them with cloud properties from the MODIS C6 product. As a result, the AHI-derived COT and CER for water cloud were correlated well with MODIS C6, with correlation coefficients of 0.77 and 0.82, respectively. The COT of the ice cloud also shows good consistency with a correlation coefficient of 0.85. It was confirmed that the CER from the AHI data is significantly larger than that of the MODIS C6. The R^2, MBE and RMSE of the ice cloud CER from the two sets of satellite data are 0.38 μm, 3.98 μm and 14.03 μm in the selected areas, respectively. The reason for the lower correlations is considered to be caused by the differences in the shapes of assumed ice particle models as well as the different single-scattering properties assumed for the retrievals from the two sets of satellite data.

The second step was the estimation of the SSR, with the input of cloud parameters derived in the first step and the AHI official aerosol

product. Sensitivity analysis of SSR to SZA, COT, AOT and surface albedo was performed to optimize the LUT in the SSR calculation algorithm. Based on the sensitivity analysis, LUT was calculated using the RSTAR model. Furthermore, a LUT-based algorithm was developed to estimate SSR by inputting the cloud and aerosol parameters and other auxiliary data (e.g. SZA, As). Finally, estimated SSR from the AHI data were validated via ground observation data. The estimated SSR was validated by 122 radiation stations at several networks, which covered the full disk regions of Himawari-8. From the validation result we confirmed that AHI estimated SSR in this study is retrieved well. The instantaneous, hourly and daily SSR from the AHI estimations is highly consistent with observed SSR. The RMSE of instantaneous SSR was 119.07 Wm^{-2}, hourly was SSR 101.86 Wm^{-2} (81.18 Wm^{-2} for CMA stations), and the daily SSR was 31.42 Wm^{-2} (26.58 Wm^{-2}). The RMSE of the hourly and daily SSR data for CMA stations is smaller than the conventional results produced by Jia et al. (2013) and Tang et al. (2016). Finally, the importance of high observation frequency SSR data is discussed. It is confirmed that SSR with 10-minute observation frequency from the AHI data is useful to improve the accuracy of SSR estimation, which is used to drive the land surface models.

In summary, high accuracy of the SSR product can be obtained through new-generation satellite sensor AHI, compared to conventional satellites. These high-resolution SSR data are important for solar energy applications and for the driving of land surface and hydrological models.

CRediT author statement

- Husi Letu: Conceptualization, Methodology, writing- original draft preparation.
- Kun Yang, Run Ma, Tianxing Wang, Huazhe Shang, Takashi Y. Nakajima, Hiroshi Ishimoto, Takashi M. Nagao: Methodology, validations, writing- original draft preparation.
- Jérôme Riedi, Anthony J. Baran, Pradeep Khatri, Liangfu Chen, Chunxiang Shi, Jiancheng Shi: Results validations, investigation, reviewing and editing.

Declaration of competing interest

The authors declare that they have no known competing financial interests or personal relationships that could have appeared to influence the work reported in this paper.

Acknowledgments

References

Bao, S., Letu, H., Zhao, C., Tana, G., Shang, H., Wang, T., Bi, L., Bao, Y., Purevjav, G., He, J., 2018. Spatiotemporal distributions of cloud parameters and the temperature response over the Mongolian Plateau during 2006–2015 based on MODIS data. IEEE Journal of Selected Topics in Applied Earth Observations and Remote Sensing 1–10.

Baran, A.J., Labonnote, L., 2007. A self-consistent scattering model for cirrus. I: the solar region. Q.J.R. Meteorol. Soc. 133, 1899–1912. https://doi.org/10.1002/qj.164.

Baran, A.J., Cotton, R., Furtado, K., Havemann, S., Labonnote, L.C., Marenco, F., Thelen, J.C., 2014. A self-consistent scattering model for cirrus. II: the high and low frequencies. Q. J. R. Meteorol. Soc. 140, 1039–1057.

Baum, B.A., Soulen, P.F., Strabala, K.I., King, M.D., Ackerman, S.A., Menzel, W.P., Yang, P., 2000. Remote sensing of cloud properties using MODIS Airborne Simulator imagery during SUCCESS. II. Cloud thermodynamic phase. J. Geophys. Res. 105 (11), 781–11,792.

Bessho, K., Date, K., Hayashi, M., Ikeda, A., Imai, T., Inoue, H., Kumagai, Y., Miyakawa, T., Murata, H., Ohno, T., 2016. An introduction to Himawari-8/9—Japan's new-generation geostationary meteorological satellites. Journal of the Meteorological Society of Japan. Ser. II 94, 151–183.

Bisht, G., Venturini, V., Islam, S., Jiang, L., 2005. Estimation of the net radiation using MODIS data for clear sky days. Remote Sens. Environ. 97, 52–67.

Bruhwiler, L., Dlugokencky, E., 1970. NOAA, Earth System Research Laboratory (ESRL) Global Monitoring Division, Boulder, CO, USA. Arctic.noaa.gov.

C.-Labonnote, L., Brogniez, G., Doutriaux-Boucher, M., Buriez, J.C., Gayet, J.F., Chepfer, H., 2000. Modeling of light scattering in cirrus clouds with inhomogeneous hexagonal monocrystals. Comparison with in-situ and ADEOS-POLDER measurements. Geophys. Res. Lett. 27, 113–116.

C.-Labonnote, L., Brogniez, G., Buriez, J., Doutriauxboucher, M., Gayet, J., Macke, A., 2001. Polarized light scattering by inhomogeneous hexagonal monocrystals: validation with ADEOS-POLDER measurements. J. Geophys. Res. 106, 12139–12153.

Cano, D., Monget, J.M., Albuisson, M., Guillard, H., Regas, N., Wald, L., 1986. A method for the determination of the global solar radiation from meteorological satellite dat. Sol. Energy 37 31–29.

Damiani, A., Irie, H., Horio, T., Takamura, T., Khatri, P., Takenaka, H., ... Cordero, R.R., 2018. Evaluation of Himawari-8 surface downwelling solar radiation by SKYNET observations. Atmos. Meas. Tech. Discuss 11, 2501–2521.

Dedieu, G., Deschamps, P.Y., Kerr, Y.H., 1987. Satellite estimation of solar irradiance at the surface of the earth and of surface albedo using a physical model applied to Metcosat data. J. Appl. Meteorol. 26, 79–87.

Doutriaux-Boucher, M., Buriez, J.-C., Brogniez, G., C.-Labonnote, L., Baran, A.J., 2000. Sensitivity of retrieved POLDER directional cloud optical thickness to various ice particle models. Geophys. Res. Lett. 27, 109–112.

Driemel, A., Augustine, J., Behrens, K., Colle, S., Cox, C., Cuevas-Agulló, E., Denn, F.M., Duprat, T., Fukuda, M., Grobe, H., Haeffelin, M., Hodges, G., Hyett, N., Ijima, O., Kallis, A., Knap, W., Kustov, V., Long, C.N., Longenecker, D., Lupi, A., Maturilli, M., Mimouni, M., Ntsangwane, L., Ogihara, H., Olano, X., Olefs, M., Omori, M., Passamani, L., Pereira, E.B., Schmithüsen, H., Schumacher, S., Sieger, R., Tamlyn, J., Vogt, R., Vuilleumier, L., Xia, X., Ohmura, A., König-Langlo, G., 2018. Baseline Surface Radiation Network (BSRN): structure and data description (1992–2017). Earth Syst. Sci. Data 10, 1491–1501.

Duarte, H.F., Dias, N.L., Maggiotto, S.R., 2006. Assessing daytime downward longwave radiation estimates for clear and cloudy skies in Southern Brazil. Agric. For. Meteorol. 139, 171–181.

Dubayah, R., 1992. Estimating net solar radiation using Landsat Thematic Mapper and digital elevation data. Water Resour. Res. 28, 2469–2484.

He, T., Liang, S., Wang, D., Shi, Q., Goulden, M.L., 2015. Estimation of high-resolution land surface net shortwave radiation from AVIRIS data: algorithm development and preliminary results. Remote Sens. Environ. 167, 20–30.

Holben, B.N., Eck, T.F., Slutsker, I., Tanre, D., Buis, J.P., Setzer, A., ... Lavenu, F., 1998. AERONET—A federated instrument network and data archive for aerosol characterization. Remote Sens. Environ. 66 (1), 1–16.

Huang, G., Ma, M., Liang, S., Liu, S., Li, X., 2011. A LUT-based approach to estimate surface solar irradiance by combining MODIS and MTSAT data. Journal of Geophysical Research Atmospheres 116.

Huang, G., Li, X., Huang, C., Liu, S., Ma, Y., Chen, H., 2016a. Representativeness errors of point-scale ground-based solar radiation measurements in the validation of remote sensing products. Remote Sens. Environ. 181, 198–206.

Huang, J., Yu, H., Guan, X., Wang, G., Guo, R., 2016b. Accelerated dryland expansion under climate change. Nat. Clim. Chang. 6.

Illingworth, A.J., Barker, H.W., Beljaars, A., Ceccaldi, M., Chepfer, H., Clerbaux, N., ... Fukuda, S, 2015. The EarthCARE satellite: The next step forward in global measurements of clouds, aerosols, precipitation, and radiation. Bulletin of the American Meteorological Society 96 (8), 1311–1332.

Ishida, H., Nakajima, T.Y., 2009. Development of an unbiased cloud detection algorithm for a spaceborne multispectral imager. Journal of Geophysical Research: Atmospheres 114 (D7).

Ishida, H., Oishi, Y., Morita, K., Moriwaki, K., Nakajima, T.Y., 2018. Development of a support vector machine based cloud detection method for MODIS with the adjustability to various conditions. Remote Sens. Environ. 205, 390–407.

Ishimoto, H., Zaizen, Y., Uchiyama, A., Masuda, K., Mano, Y., 2010. Shape modeling of mineral dust particles for light-scattering calculations using the spatial Poisson-Voronoi tessellation. J. Quant. Spectrosc. Radiat. Transf. 111, 2434–2443.

Ishimoto, H., Masuda, K., Mano, Y., Orikasa, N., Uchiyama, A., 2012. Irregularly shaped ice aggregates in optical modeling of convectively generated ice clouds. J. Quant. Spectrosc. Radiat. Transf. 113, 632–643.

Jia, B., Xie, Z., Dai, A., Shi, C., Chen, F., 2013. Evaluation of satellite and reanalysis products of downward surface solar radiation over East Asia: spatial and seasonal variations. Journal of Geophysical Research: Atmospheres 118, 3431–3446.

Kawamoto, K., Nakajima, T., Nakajima, T.Y., 2001. A global determination of cloud microphysics with AVHRR remote sensing. J. Clim. 14, 2054–2068.

Kikuchi, M., Murakami, H., Suzuki, K., Nagao, T.M., Higurashi, A., 2018. Improved hourly estimates of aerosol optical thickness using spatiotemporal variability derived from Himawari-8 geostationary satellite. IEEE Trans. Geosci. Remote Sens. 56, 3442–3455.

Kim, H.Y., Liang, S., 2010. Development of a hybrid method for estimating land surface shortwave net radiation from MODIS data. Remote Sens. Environ. 114, 2393–2402.

Klink, J.C., Dollhopf, K.J., 1986. An evaluation of satellite-based insolation estimates for Ohio. J. Appl. Meteorol. 25, 1741–1751.

Letu, H., Nakajima, T.Y., Matsui, T.N., 2012. Development of the ice crystal scattering database for the GCOM-C/SGLI satellite mission: investigating the refractive index grid system and potential retrieval error. Appl. Opt. 51, 6172–6178.

Letu, H., Nagao, T.M., Nakajima, T.Y., Matsumae, Y., 2014. Method for validating cloud

mask obtained from satellite measurements using ground-based sky camera. Appl. Opt. 53 (31), 7523–7533.

Letu, H., Ishimoto, H., Riedi, J., Nakajima, T.Y., C.-Labonnote, L., Baran, A.J., Nagao, T.M., Sekiguchi, M., 2016. Investigation of ice particle habits to be used for ice cloud remote sensing for the GCOM-C satellite mission. Atmos. Chem. Phys. 16 (18), 12287–12303.

Letu, H., Nagao, T.M., Nakajima, T.Y., Riedi, J., Ishimoto, H., Baran, A.J., Shang, H., Sekiguchi, M., Kikuchi, M., 2018. Ice cloud properties from Himawari-8/AHI next-generation geostationary satellite: capability of the AHI to monitor the DC cloud generation process. IEEE Trans. Geosci. Remote Sens. 1–11.

Li, Z., Leighton, H.G., Masuda, K., Takashima, T., 1993. Estimation of SW flux absorbed at the surface from TOA reflected flux. J. Clim. 6, 317–330.

Li, Y., Yu, R., Xu, Y., Zhang, X., 2004. Spatial distribution and seasonal variation of cloud over China based on ISCCP data and surface observations. J. Meteorol. Soc. Jpn. 82, 761–773.

Liang, S., Zheng, T., Liu, R., Fang, H., Tsay, S.C., Running, S., 2006. Estimation of incident photosynthetically active radiation from Moderate Resolution Imaging Spectrometer data. Journal of Geophysical Research Atmospheres 111.

Lu, N., Qin, J., Yang, K., Sun, J., 2011. A simple and efficient algorithm to estimate daily global solar radiation from geostationary satellite data. Energy 36, 3179–3188.

Mangum, L., 1998. The Tropical Atmosphere Ocean (TAO) array world wide web site. Argos Newsletter 53, 9–11.

Masuda, K., Ishimoto, H., Mano, Y., 2012. Efficient method of computing a geometric optics integral for light scattering. Meteorology and Geophysics 63, 15–19.

Mei, L., Rozanov, V., Vountas, M., Burrows, J.P., 2018. The retrieval of ice cloud parameters from multi-spectral satellite observations of reflectance using a modified XBAER algorithm. Remote Sens. Environ. 215, 128–144.

Nakajima, T.Y., Nakajma, T., 1995. Wide-area determination of cloud microphysical properties from NOAA AVHRR measurements for FIRE and ASTEX regions. J. Atmos. Sci. 52, 4043–4059.

Nakajima, T., Tanaka, M., 1986. Matrix formulations for the transfer of solar radiation in a plane-parallel scattering atmosphere. J. Quant. Spectrosc. Radiat. Transf. 35, 13–21.

Nakajima, T., Tanaka, M., 1988. Algorithms for radiative intensity calculations in moderately thick atmospheres using truncation approximation. J. Quant. Spectrosc. Radiat. Transf. 40, 51–69.

Nakajima, T.Y., Ishida, H., Nagao, T.M., Hori, H., Letu, H., Higuchi, R., Tamaru, N., Imoto, N., Yamazaki, A., 2019. Theoretical basis of the algorithm and early phase results of the GCOM-C (Shikisai) SGLI cloud products. Progress in Earth and Planetary Science. https://doi.org/10.1186/s40645-019-0295-9.

Okuyama, A., Takahashi, M., Date, K., Hosaka, K., Murata, H., Tabata, T., Yoshino, R., 2018. Validation of Himawari-8/AHI radiometric calibration based on two years of in-orbit data. Journal of the Meteorological Society of Japan. Ser. II 96, 91–109.

Pinker, R.T., Ewing, J.A., 1985. Modeling surface solar radiation: model formulation and validation. J. Appl. Meteorol. 24, 389–401.

Pinker, R.T., Laszlo, I., Tarpley, J.D., Mitchell, K.E., 2002. Geostationary satellite parameters for surface energy balance. Adv. Space Res. 30, 2427–2432.

Pinker, R.T., Tarpley, J.D., Laszlo, I., Mitchell, K.E., Houser, P.R., Wood, E.F., Schaake, J.C., Robock, A., Lohmann, D., Cosgrove, B.A., 2003. Surface radiation budgets in support of the GEWEX Continental-Scale International Project (GCIP) and the GEWEX Americas Prediction Project (GAPP), including the North American Land Data Assimilation System (NLDAS) project. Journal of Geophysical Research Atmospheres 108, GCP5-1.

Platnick, S., King, M.D., Ackerman, S.A., Menzel, W.P., Baum, B.A., Riédi, J.C., Frey, R.A., 2003. The MODIS cloud products: algorithms and examples from Terra. IEEE Trans. Geosci. Remote Sens. 41 (2), 459–473.

Platnick, S., Meyer, K.G., King, M.D., Wind, G., Amarasinghe, N., Marchant, B., ... Yang, P., 2017. The MODIS cloud optical and microphysical products: Collection 6 updates and examples from Terra and Aqua. IEEE Transactions on Geoscience and Remote Sensing 55 (1), 502–525.

Qin, J., Tang, W., Yang, K., Lu, N., Niu, X., Liang, S., 2015. An efficient physically based parameterization to derive surface solar irradiance based on satellite atmospheric products. Journal of Geophysical Research Atmospheres 120, 4975–4988.

Rigollier, C., Bauer, O., Wald, L., 2000. On the clear sky model of the ESRA—European Solar Radiation Atlas—with respect to the Heliosat method. Sol. Energy 68 (1), 33–48.

Rigollier, C., Lefèvre, M., Wald, L., 2004. The method Heliosat-2 for deriving shortwave solar radiation from satellite images. Sol. Energy 77 (2), 159–169.

Schmit, T.J., Gunshor, M.M., Menzel, W.P., Gurka, J.J., Li, J., Bachmeier, A.S., 2005. Introducing the next-generation advanced baseline imager on Goes-R. Bull. Am. Meteorol. Soc. 86, 1079–1096.

Sekiguchi, M., Nakajima, T., 2008. A k-distribution-based radiation code and its computation optimization for an atmospheric general circulation model. J. Quant. Spectrosc. Radiat. Transf. 109, 2779–2793.

Shang, H., Chen, L., Letu, H., Zhao, M., Li, S., Bao, S., 2017. Development of a daytime cloud and haze detection algorithm for Himawari-8 satellite measurements over central and eastern China. Journal of Geophysical Research: Atmospheres 122 (6), 3528–3543.

Shang, H., Letu, Pan, X., Wang, Z., Ma, R., Liu, C., ... Hu, Q., 2019. Diurnal haze variations over the North China plain using measurements from Himawari-8/AHI. Atmospheric Environment 210, 100–109.

Sridhar, V., Elliott, R.L., 2002. On the development of a simple downward longwave radiation scheme. Agric. For. Meteorol. 112, 237–243.

Takenaka, H., Nakajima, T.Y., Higurashi, A., Higuchi, A., Takamura, T., Pinker, R.T., Nakajima, T., 2011. Estimation of solar radiation using a neural network based on radiative transfer. Journal of Geophysical Research Atmospheres 116, 353–366.

Tang, B., Li, Z., 2008. Estimation of instantaneous net surface longwave radiation from MODIS cloud-free data. Remote Sens. Environ. 112, 3482–3492.

Tang, B., Li, Z.L., Zhang, R., 2006. A direct method for estimating net surface shortwave radiation from MODIS data. Remote Sens. Environ. 103, 115–126.

Tang, W., Qin, J., Yang, K., Liu, S., Lu, N., Niu, X., 2016. Retrieving high-resolution surface solar radiation with cloud parameters derived by combining MODIS and MTSAT data. Atmos. Chem. Phys. 16, 2543–2557.

Tarpley, J.D., 1979. Estimating incident solar radiation at the surface from geostationary satellite data. J. Appl. Meteorol. 18, 1172–1181.

Wang, W., Liang, S., 2009. Estimation of high-spatial resolution clear-sky longwave downward and net radiation over land surfaces from MODIS data. Remote Sens. Environ. 113, 745–754.

Wang, T., Pinker, R.T., 2009. Shortwave radiative fluxes from MODIS: model development and implementation. Journal of Geophysical Research Atmospheres 114.

Wang, T., Yan, G., Chen, L., 2012. Consistent retrieval methods to estimate land surface shortwave and longwave radiative flux components under clear-sky conditions. Remote Sens. Environ. 124, 61–71.

Wang, D., Liang, S., He, T., Shi, Q., 2015. Estimation of daily surface shortwave net radiation from the combined MODIS data. IEEE Trans. Geosci. Remote Sens. 53 (10), 5519–5529.

Warren, S.G., Brandt, R.E., 2008. Optical constants of ice from the ultraviolet to the microwave: a revised compilation. J. Geophys. Res. 113, D14220. https://doi.org/10.1029/2007JD009744.

Wild, M., 2009. Global dimming and brightening: a review. Journal of Geophysical Research Atmospheres 114.

Wild, M., 2012. New directions: a facelift for the picture of the global energy balance. Atmos. Environ. 55, 366–367.

Xue, B., Wang, L., Li, X., Yang, K., Chen, D., Sun, L., 2013. Evaluation of evapotranspiration estimates for two river basins on the Tibetan Plateau by a water balance method. J. Hydrol. 492, 290–297.

Yan, G., Wang, T., Jiao, Z., Mu, X., Zhao, J., Chen, L., 2016. Topographic radiation modeling and spatial scaling of clear-sky land surface longwave radiation over rugged terrain. Remote Sens. Environ. 172, 15–27.

Yang, P., Liou, K.N., Wyser, K., Mitchell, D., 2000. Parameterization of the scattering and absorption properties of individual ice crystals. Journal of Geophysical Research: Atmospheres 105, 4699–4718.

Yang, P., Gao, B.-C., Baum, B.A., Hu, Y.X., Wiscombe, W.J., Tsay, S.-C., Winker, D.M., Nasiri, S.L., 2001a. Radiative properties of cirrus clouds in the infrared (8–13 mm). J. Quant. Spectrosc. Radiat. Transf. 70, 473–504.

Yang, K., Huang, G.W., Tamai, N., 2001b. A hybrid model for estimating global solar radiation. Sol. Energy 70, 13–22.

Yang, P., Wei, H., Huang, H.-L., Baum, B.A., Hu, Y.X., Kattawar, G.W., Mishchenko, M.I., Fu, Q., 2005. Scattering and absorption property database for nonspherical ice particles in the near- through far-infrared spectral region. Appl. Opt. 44, 5512–5523.

Yang, K., Koike, T., Ye, B., 2006. Improving estimation of hourly, daily, and monthly solar radiation by importing global data sets. Agric. For. Meteorol. 137, 43–55.

Yang, P., Bi, L., Baum, B.A., Liou, K.N., Kattawar, G.W., Mishchenko, M.I., Cole, B., 2013. Spectrally consistent scattering, absorption, and polarization properties of atmospheric ice crystals at wavelengths from 0.2 to 100 μm. J. Atmos. Sci. 70, 330–347.

Yoshida, M., Kikuchi, M., M, N.T., Murakami, H., Nomaki, T., Higurashi, A., 2018. Common retrieval of aerosol properties for imaging satellite sensors. Journal of the Meteorological Society of Japan. Ser. II. 96B, 193–209.

Zhang, X., Liang, S., Wild, M., Jiang, B., 2015. Analysis of surface incident shortwave radiation from four satellite products. Remote Sens. Environ. 165, 186–202.

Zheng, T., Liang, S., Wang, K., 2008. Estimation of incident photosynthetically active radiation from GOES visible imagery. J. Appl. Meteorol. Climatol. 47, 853–868.

Zhou, Y., Cess, R.D., 2001. Algorithm development strategies for retrieving the downwelling longwave flux at the Earth's surface. Journal of Geophysical Research: Atmospheres 106, 12477–12488.

Zhou, Y., Kratz, D.P., Wilber, A.C., Gupta, S.K., Cess, R.D., 2007. An improved algorithm for retrieving surface downwelling longwave radiation from satellite measurements. Journal of Geophysical Research: Atmospheres 112.